ELLIPSOMETRIC ANALYSIS OF SILICON NANOPARTICLES FORMED BY THERMAL ANNEALING

THESIS

Presented to the Graduate Council of
Texas State University-San Marcos
in Partial Fulfillment
of the Requirements

for the Degree

Master of SCIENCE

by

Chad Lawrence Waxler, B.A.

San Marcos, Texas
May 2013

ELLIPSOMETRIC ANALYSIS OF SILICON NANOPARTICLES FORMED BY

THERMAL ANNEALING

Committee Members Approved:

_____
Gregory Spencer, Chair

_____
Wilhelmus Geerts

_____
Ravindranath Droopad

_____
J. Michael Willoughby
Dean of the Graduate College

FAIR USE AND AUTHOR'S PERMISSION STATEMENT

Fair Use

Duplication Permission

ACKNOWLEDGEMENTS

TABLE OF CONTENTS

vii

LIST OF TABLES

LIST OF FIGURES

Page

ABSTRACT

ELLIPSOMETRIC ANALYSIS OF SILICON NANOPARTICLES FORMED BY
THERMAL ANNEALING

by

Chad Lawrence Waxler, B.A.

Texas State University-San Marcos

May 2013

SUPERVISING PROFESSOR: Gregory Spencer

In this study, we investigate the surface morphology and optical properties of silicon nanoparticles formed on a silicon-on-insulator substrate by thermal annealing of a thin silicon layer. The annealing is performed using a rapid thermal annealer in an argon environment at atmospheric pressure. We analyze the formation of silicon nanoparticles as a function of silicon layer thickness, annealing temperature, and annealing duration using Atomic Force Microscopy (AFM) and we analysis the optical properties via Effective Medium Approximations (EMA) models using a Variable Angle Spectroscopic Ellipsometer (VASE). The results of these experiments showed that samples with a smaller initial silicon layer thicknesses produce larger average particle size and have a wider distribution of sizes than samples with thicker silicon top layers. As the annealing temperature and duration increases, so does the average nanoparticle radius. Analysis of the oxidation of the nanoparticles revealed that samples which exhibited a narrow distribution of small nanoparticles sizes oxidizes to a lesser extent than those with larger particles and wider distributions.

CHAPTER 1

INTRODUCTION

Silicon is an important material for many areas of technology including microchips, micromechanic sensors and actuators, and solar energy conversion. Integrated circuits (ICs) are made from circuits of transistors which are composed of predominantly silicon; micromechanical sensors and actuators are produced out of silicon wafers using anisotropic wet etching technologies; solar cells are fabricated from poly-crystalline or crystalline silicon. Silicon is known as an intrinsic semiconductor because at any temperature above absolute zero temperature, there is a finite probability that an electron in the lattice will be knocked loose from its position, leaving behind an electron deficiency called a hole. These electrons which are excited across the band gap into the conduction band are mobile and can support charge transport. The holes left behind in the valence band are also mobile and also contribute to charge transport in the material.

Silicons wide ranging uses in the semiconductor industry are due to the fact that it can remains a semiconductor at higher temperatures than the semiconductor germanium and because its native oxide is easily grown in a furnace and forms an excellent passivated semiconductor/dielectric interface.[1]

Bulk silicon crystal is the main material of today's microelectronic, photovoltaic, and MEMS technologies, but recent trends in research have been to also study the usefulness of nanocrystalline silicon. Reducing the size of the silicon crystals to the nanoscale level brings about new properties and functionalities and are expected to pave the way for new and exiting applications in microelectronic, photonic,

photovoltaic, and nanobiotech industries.[2]

The very small size of the grains leads to strong electron and hole confinement modifying the electronic structure of the silicon. It forms naturally a system of quantum-dots (QDs) over a large area without the need for high-resolution lithographic definition of the dots.[3] This small grain size also makes nanocrystaline films promising for use as quantum-dot transistors or single electron transistors.[4] To utilize the quantum confinement effects for devices intended for room temperature operations, the size of the quantum dots has to be on the order of 10nm. Creating features of this size presents a challenge to nanofabrication technology, even for the new approaches using scanning probe microscopy.[5]

The objective of this research is to investigate the surface morphology, oxidation state, and optical properties of silicon nanoparticles formed on a silicon-on-insulator (SOI) substrate by thermal annealing as a function of silicon layer thickness and annealing temperature and duration. Silicon nanoparticles were created by sputtering silicon layers with thicknesses of 3, 6, or 9 nm which were then thermally annealed at atmospheric pressure in an argon environment with annealing durations from 30 - 120 seconds.

In Chapter 2 of this thesis, I discuss previous work that has been done regarding silicon nanoparitcle formation and their results. In Chapter 3, I discuss the equipment that was used during this research as well as general background to how the equipment works. Chapter 4 describes the procedure that was used to create all of the samples for this study. Chapter 5 and 6 contains the results of the nanoparticle analysis and the conclusions drawn from these results.

CHAPTER 2

PREVIOUS WORK

Since the observation of room temperature luminescence and quantum size effects in silicon nanoparticles in 1990, research in silicon nanoparticles has greatly increased. Various methods of nanoparticle formation have shown promising results, such as gas and liquid phase processes, non-thermal plasmas, laser ablation, and thermal annealing.[6]

For this thesis, the focus will be on the relatively simple method of nanoparticle formation by the thermal annealing of a thin silicon layer on an inert surface such as silicon dioxide in an inert atmosphere. This method has been used by other groups with promising results.

In one study,[7] a 10 nm amorphous silicon layer was deposited by electron-beam evaporation on a mirror-polished quartz glass (SiO_2) substrate which was then annealed in a high vacuum. The temperatures of the samples were elevated by 15°C per minute until they had reached maximum temperatures of 550, 575, and 600°C and were then held at that temperature for 30 minutes before being allowed to cool to room temperature. Analysis of the samples by the use of a transmission electron microscope (TEM) revealed that round crystalline islands (or nanoparticles) started to form randomly on the sample at 550°C and as the maximum annealing temperature increased, so did the number of the nanoparticles. At a temperature of 575°C a single distribution of widely spaced nanoparticles with an average radius of 32.1 nm were observed. Annealing at a temperature of 600°C led to the formation of relatively small islands ranging from 15 to 25 nm in radius. This group also

created nanoparticles by annealing a 1.5 nm silicon layer at 600°C, forming nanoparticles with radii of 7 to 14 nm. The formation of the silicon nanoparticles is explained thermodynamically through the minimization of the free energy of the amorphous-crystalline transition and the competing surface energies between the amorphous, crystalline, and oxidized silicon films.[8]

In another UHV study,[5,9] samples are made from a SOI substrate with a top layer of crystalline silicon in the range of thicknesses from 6 to 19 nm. To create samples with a thinner top layer, some samples were thinned chemically using hydrofluoric acid down to a thickness of 3 nm. This process allowed for the thinning of the silicon top layer while maintaining it's crystallinity. To create even thinner top layers down to 1 nm thicknesses, argon ion milling was used creating an amorphous silicon layer. The samples were resistively heated through the silicon wafer in an ultrahigh vacuum with maximum temperatures ranging from 500 to 900°C. Due to the resistive heating, the samples were quickly heated to the maximum temperature (within 10 seconds) and held there for 10 minutes. Using *in situ* Auger electron spectroscopy, a minimum formation temperature of the silicon nanoparticles was observed that depended on the initial silicon top layer thickness. Samples with a top crystalline silicon layer thickness of 3 to 19 nm showed nanoparticle formation at temperatures in the range of 825 to 875°C, while samples with an amorphous silicon layer 1 nm thick showed nanoparticles at temperatures as low as 570°C.

In another study,[8] silicon nanoparticles were created by annealing at atmospheric pressure in an inert gas. For this study, samples were created by sputtering 6 and 15 nm layers of amorphous silicon on top of a thermally grown SiO_2 layer. After sputtering, these samples were annealed using a rapid thermal annealer in an argon environment with maximum temperatures ranging from 600 to 900°C. Annealing was done with a duration of 30 seconds for the 6 nm layer and 60

seconds for the 15 nm layer. The samples were analyzed using atomic force microscopy and silicon nanoparticle formation was observed at all temperatures, including the minimum annealing temperature of 600°C. The nanoparticles created in this study were formed in a close packed arrangement, unlike the well spaced nanoparticles of the UHV studies. This study also differed from the UHV studies by showing nanoparticle formation at much lower temperatures for their silicon top layer thickness than those of the UHV studies.

The studies listed so far have dealt primarily with the formation of silicon nanoparticles in terms of particle size and distribution, but have not analyzed the composition of the particles. In a study performed by S. J. Fang *et al.*,[10] efforts were made to analyze silicon samples with different surface roughness. The effect of surface roughness on the ellipsometric quantities was investigated and compared to the results of roughness data obtained from AFM measurements. For that research, two groups of samples were prepared by cleaving a silicon substrate into 55 samples, i.e. wet etched samples, and thermally processed samples. The wet etched samples were roughened using a standard preoxidation clean, a HF/hot water sequence, or a buffered-oxide-etch. Thermally processed samples were wet-etched first, then oxidized, and the then stripped with dilute HF. Ellipsometric data were collected within 2 min after HF dipping followed by AFM analysis. From this work they found that, although the wet etched and the thermally processed samples have similar root mean square (RMS) roughness values, the volume fraction of the roughness can be very different. The silicon volume fractions of the wet etched and thermally processed groups are about 40-60% and 70-90%, respectively. Due to this, in order to correctly model the Si/SiO_2 interface roughness, the researchers assumed a volume fraction of silicon of 50% for the wet etched samples and 80% for the thermally processed samples. They also found that this interface layer thickness is equal to approximately 1.71 of the RMS value as measured by an atomic force

microscope.

In further studies,[11–13] the oxidation kinetics of various sized nanoparticles have been studied under various conditions. In one of these studies,[11] crystalline silicon nanoparticles with diameters of 20 - 500 nm were prepared by the gas-evaporation method with a pulsed laser in an argon atmosphere and then subjected to high temperature oxidation. The oxidation of the silicon nanoparticles was performed in a mixture of argon and oxygen gasses (Ar-20%O_2) at atmospheric pressure with temperatures ranging from 1123-1273 K and duration from 30 minutes to 3 hours. The oxide layer thickness and the diameter of the oxidized particles were determined by high-resolution transmission electron microscopy (TEM). In another study,[12] laser-induced decomposition of silane was used for the fabrication of silicon nanoparticles with sizes of 6 - 33 nm and a TEM was used to monitor the room temperature oxidation of these particles. Both of these studies found a slower oxidation rate for small Si particles in air and at high temperature. This slowing of the oxidation rate for small particles has been attributed to stress-induced suppression of the oxidization process.

CHAPTER 3

EQUIPMENT

3.1   Instruments

For this research, the primary equipment used included an RF magnetron sputtering system with a substrate heater, an atomic force microscope (AFM), a rapid thermal annealer (RTA), a variable angle spectroscopic ellipsometer (VASE), and ellipsometery analysis software CompleteEASE. The RF magnetron sputtering system was used to sputter a thin silicon layers on top of the SiO_2 covered silicon wafer. After sputtering, the samples were then annealed in either ultra-high vacuum (UHV) inside the RF magnetron sputtering chamber or at atmospheric pressure in an argon environment inside the RTA. After annealing, the samples were analyzed using a VASE to determine their composition and roughness. Finally, the samples were analyzed using AFM to determine nanoparticle size and distribution.

3.2   RF Magnetron Sputtering

Sputtering is a method of deposition whereby atoms are ejected from a solid target material due to bombardment of the target by energetic particles.[14] The general configuration for sputtering, is a substrate placed opposite of a source material in an evacuated chamber. The source material is referred to as the target. An inert gas, such as argon, is let into the chamber and a sufficiently high voltage is applied between the target and the substrate material creating a plasma. Inside the plasma the argon atoms are hit by free electrons. The atoms become positively

charged ion and secondary electrons are created. The positive ions created by the plasma are continuously accelerated to the negatively charged target surface. These accelerated argon ions will act like atomic-sized abrasive grit (like a sand blaster) and cause atomic size particles to be ejected from the target. Subsequently these atomic particles will be deposited on the substrate.

In magnetron sputtering, strong magnets are incorporated under the target material. The strong magnetic fields of the magnet are utilized to increase the path length of the charges in the plasma and confine charged plasma particles close to the surface of the sputter target. In a magnetic field, electrons follow helical paths around the magnetic field lines undergoing more ionizing collisions with gaseous neutral argon atoms near the target surface than would otherwise occur. The extra argon ions created as a result of these collisions leads to a higher deposition rate. It also means that the plasma can be sustained at a lower pressure. The sputtered atoms are mostly neutral and are therefore unaffected by the magnetic trap.[15]

Sputtering is used extensively in the semiconductor industry to deposit thin films of various materials and offers some important advantages compared to other methods. For example, sputtering allows for deposition of materials with high melting points that would be difficult to use with other processes that require thermal evaporation. Another important advantage of sputtering is that the plasma creates a directional beam of atoms, so material is not deposited all over in the vacuum system but only in the area of the substrate. This will reduce the number of required cleaning cycles and will make a more efficient use of source material.

There are several types of sputtering: here I mention direct current (DC) sputtering and radio frequency (RF) sputtering. The configuration for DC and RF sputtering are similar and are shown in Figure 3.1.

The main difference between the two configurations is the ability to sputter insulators with RF sputtering. If the source material is an insulator and the DC
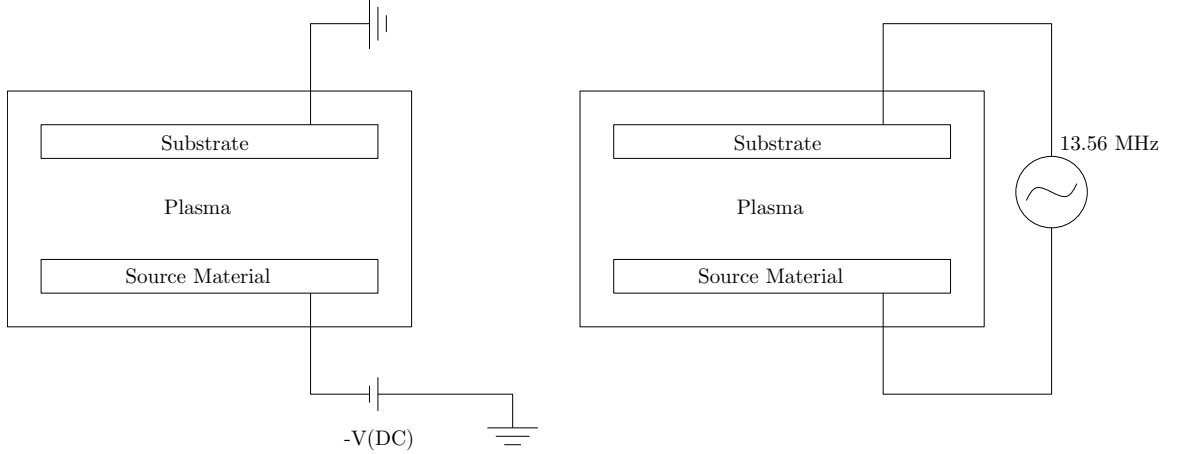
Figure 3.1: Simplified Schematic of Sputtering. Simplified schematic of a DC (left) and RF (right) sputtering system.

configuration is used, then positive charge will build up on the target and this will interfere with the sputtering process. Charge build-up on insulating targets can be avoided with the use of RF sputtering where the sign of the anode-cathode bias is varied at a high rate (commonly 13.56 MHz).[16] For this research, we used an AJA International ATC Orion Magnetron Sputtering System in a RF configuration to sputter a thin films of silicon on top of an SiO_2 covered silicon wafer. An image of the AJA system is shown in Figure 3.2.

3.3 Rapid Thermal Annealer (RTA)

Rapid thermal processing refers to a semiconductor manufacturing process which heats silicon wafers to high temperatures (up to 1200°C or greater) on a timescale of several seconds or less using high power lamps. RTA was originally developed for the semiconductor industry to anneal wafers to activate dopants and or repair damage of ion implantation. The ability of RTA to heat up and cool down samples very rapidly, allows for a very controllable annealing process that has a large throughput. RTA is now also applied for other process steps including the change of film-to-film or film-to-wafer substrate interfaces, the change of the density of
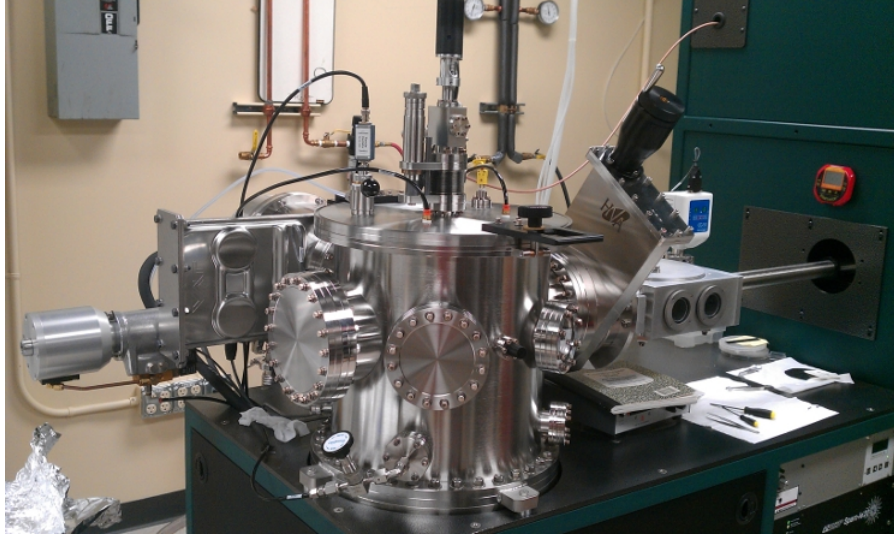
Figure 3.2: Picture of the AJA International Sputtering System.

deposited films, the change of the states of grown films, and to move dopants or to drive dopants from one film into another.[17]

For this research an AG Associates Heatpulse 610 rapid thermal annealer was used to heat our samples to temperatures of 600-800° C for 30-120 seconds. For each sample, the temperature was ramped from room temperature to the maximum annealing temperature at a rate of approximately 150° C per minute. The Heatpulse 610 heats the samples placed inside of a quartz chamber by using high-powered tungsten halogen lamps. Before annealing, the chamber is flushed with ultra-high purity argon for 2 minutes at a rate of approximately 5 liters per minute. This argon flow continues during the entire annealing process until the sample is back to nearly room temperature to minimize oxidation.

To control the temperature, the Heatpulse 610 has the option for either a thermocouple or an extended range pyrometer. For annealing samples at or below 600°C, the thermocouple provides better accuracy. For higher temperatures, the pyrometer is the better option. For consistency with our samples, the pyrometer was used to control the temperature for our samples.

3.4   Variable Angle Spectroscopic Ellipsometer

In general, ellipsometry is a non-destructive technique that uses reflected light to gather information about thin film composition and thickness. Ellipsometry measures the change in polarization state of the measurement beam induced by reflection from (or transmission through) the sample. Light is an electromagnetic wave meaning that light is composed of an oscillating electric and magnetic field that are orthogonal to each other. For purposes of ellipsometry in the visible part of the spectrum, it is adequate to discuss the wave's electric field behavior in space and time, also known as polarization. There are three types of polarized light which are known as linear, circular, and elliptical. Linearly polarized light is created when two linearly polarized orthogonal waves of light are in-phase. Circularly polarized light is created when two linearly polarized orthogonal waves of light are exactly 90°out of phase and have equal amplitude. Elliptically polarized light is the most commons polarization and is created when the two linearly polarized orthogonal waves of light have unequal amplitude and have a phase difference different from zero. These different types of polarized light are shown in Figure 3.3.

The electrical field of linearly polarized incident light can be projected into two orthogonal polarization components, as shown in Figure 3.4. One is parallel to the plane of incidence, defined by the incident beam and the direction normal to the surface, and is referred to as the p-polarized electric field component E_p. The other, perpendicular to the plane of incidence, is referred to as the s-polarized component E_s. The s-polarized and p-polarized light waves behave differently when they are reflected from the sample.[18] This is caused by different electric depolarization effects occurring at the planar interface for p- and s-polarized light. These effects are best described by the Fresnel reflection coefficients and, in general, cause linearly polarized incident light to be reflected as elliptically polarized light.
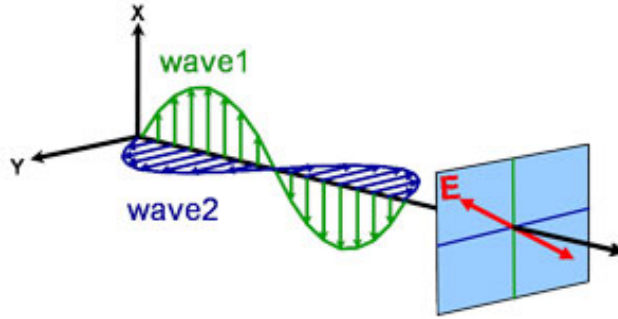
(a) Linearly Polarized Light
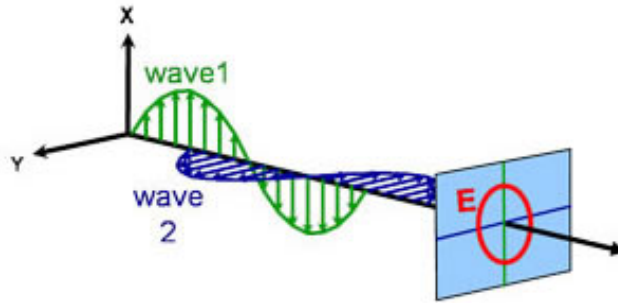
(b) Circularly Polarized Light
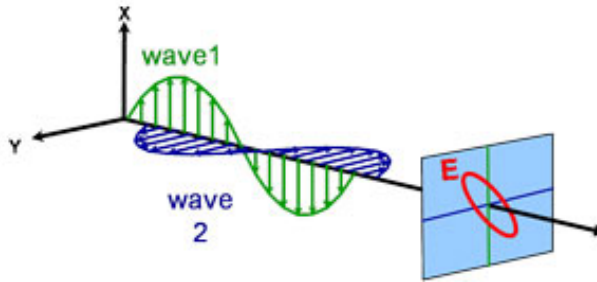
(c) Elliptically Polarized Light

Figure 3.3: Types of Polarization. Combining waves of light to create various types of polarization.

The change in polarization state upon reflection is summarized by the ellipsometric quantities Psi (Ψ) and Delta (Δ). Theses parameters are defined by Equation 3.1.

$$\tan(\Psi) \cdot e^{i\Delta} = \rho = \frac{r_p}{r_s} \tag{3.1}$$

In this equation, ρ is defined as the ratio of the complex reflectivity for

Figure 3.4: Typical Ellipsometry Configuration. Here the linearly polarized light is reflected from the sample surface and the polarization change is measured to determine the sample response.

p-polarized light (r_p) divided by the complex reflectivity for s-polarized light (r_s). ρ is a complex number, and the ellipsome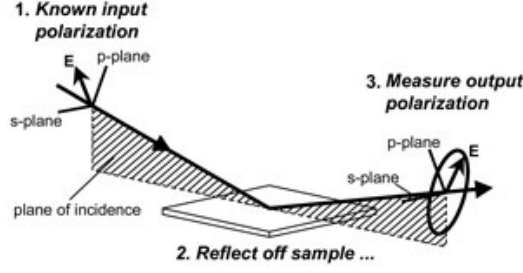tric quantities simply report this value in polar form: $\tan(\Psi)$ is the magnitude of the reflectivity ratio, and Δ is the phase shift difference between p and s-polarized light upon reflection.[19] For a bulk sample that has an infinite thickness, the Fresnel reflection coefficients can be used to relate the measured Ψ and Δ to optical properties of the sample such as the refraction index and the extinction coefficient. Often samples are not really bulk, but consist of a multilayer stack of films, some of whom consists of a mix of different materials. Although one can still derive an expression for the Ψ and Δ as a function of the sample's properties, it will be more difficult if not impossible to find an analytical expression for the inverse of that function. Therefore often an interative approach is followed if one wants to estimate certain sample properties from the measured ellipsometric quantities. More details on this approach is provided below. The Woollam ellipsometer used in this work allowed for the determination of the ellipsometric quantities at different wavelengths (215-1000 nm) and at different angles of incidence (45-90 degrees).

After the sample is measured and the Ψ and Δ data are gathered at different wavelengths and different angles of incidence, a model of the sample is created by the user. This model accurately describes what is known of the sample and consists
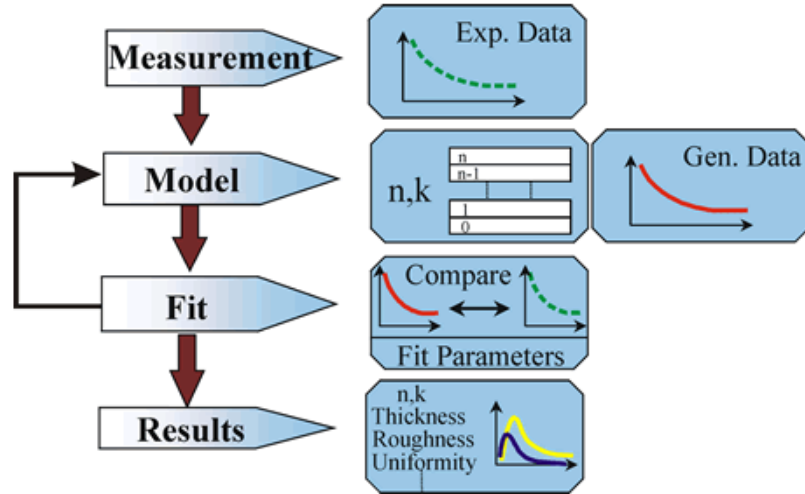
Figure 3.5: Flowchart for Ellipsometry Data Analysis.

of a list of layers the sample consist of. For each layer the model defines the thickness, the material properties and other specifics such as composition and roughness. Some of those model parameters are known from the deposition parameters or from other type of measurements on the sample and are fixed by the user. Other parameters are not known exactly. The user will give those parameters an initial value which is normally a good educated guess. Those parameters are not fixed but are to be fitted by the Woollam software. The Woollam software calculates the Ψ and Δ from the model and from specifics about the experiment, i.e. wavelength and angle of incidence. The value of the estimated layer property will then be varied until the generated data is close to the experimental data.[18] This process is repeated, as shown in the flowchart in Figure 3.5, until an acceptable model is created. The mean square error (MSE) between the fitted model and the data is calculated to guide the fit and to quantify the goodness of the fit calculated from the measurement data. The better the model, the lower the MSE, however the acceptable value of the MSE depends on the type of sample. Simple single film samples may have a MSE close to zero while more complex samples will have higher MSE values. As a single ellipsometric measurement only provides two independent

measurement values (i.e. Ψ and Δ), the number of model parameters that can be unambiguously estimated from the measurement results is normally limited to two independent parameters. Note that some model parameters are only sensitive in Δ or in Ψ which can further limit fit strategies.[10] The ellipsometer used in this thesis allows for measurements at different angles of incidence and at different wavelengths, allowing for more complex models to be evaluated.

When analyzing layer composition using spectroscopic ellipsometry, it is useful to define a layer in the model that is a mixture of two or more materials. This is known as an effective medium approximation (EMA). To use an EMA, a mixing method must be defined. The three most common mixing methods are a simple linear combination, Maxwell-Garnet EMA, and Bruggeman EMA. The Linear mixing simply interpolates between the constituents' dielectric functions to get the optical constants of the composite material. The Maxwell-Garnett assumes spherical inclusions of the second and/or third material in a host matrix of first material. The Bruggeman EMA makes the self-consistent choice of the host material. The Maxwell-Garnett and Bruggeman EMAs are very useful for modeling surface and interfacial roughness as well as modeling poly-crystalline materials by mixing together amorphous and crystalline optical constants of the material.[19]

3.5 Atomic Force Microscope

Atomic force microscopy (AFM) is a method for measuring surface properties and/or profiles with atomic-scale topographical definition.[20] An AFM gathers information about the surface of the sample by using a sharp tip built at the end of a cantilever which is vibrated near it's resonance frequency and moved parallel to the sample surface. To measure the motion of the probe over the surface a laser is pointed at the end of the cantilever and as the cantilever moves vertically, the reflected laser beam, or "return signal," is deflected in a regular pattern over a

photodiode array, generating a sinusoidal, electronic signal.[21] The sharp tip is brought atomically close to the sample allowing for van der Waals interactions between the sample and the resonating tip. These van der Waals interactions push and pull on the cantilever causing a change in the reflected laser on the photodiode. This provides information about the vertical height of the sample surface. A schematic of a typical AFM is shown in Figure 3.6.
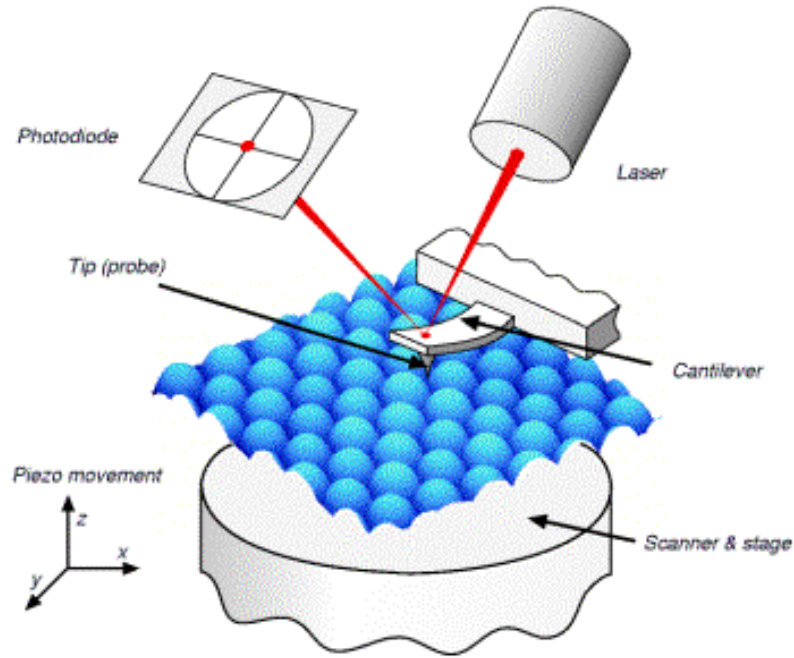
Figure 3.6: AFM Schematic. A simplified schematic of a typical AFM.

For the AFM to be able to gather information about the surface of the sample, the force between the tip and the surface must be known. The force is not measured directly, but calculated by measuring the deflection of the lever, and knowing the stiffness of the cantilever. Hook's law gives $F = -kz$, where F is the force, k is the stiffness of the lever, and z is the distance the lever is bent.[22] This force is shown in Figure 3.7.

The force curve in Figure 3.7 is also useful to show the two most common modes of operation for AFM. The first of these is known as contact mode. When in contact

Tip is in hard contact
with the surface;
repulsive regime

Tip is far from the
surface; no deflection

Force

0

Tip is pulled toward the
surface - attractive regime

Probe Distance from Sample (z distance)

Figure 3.7: AFM Force Curve. Plot of the force
bewteen the tip and the sample as a function of
the distance between them.
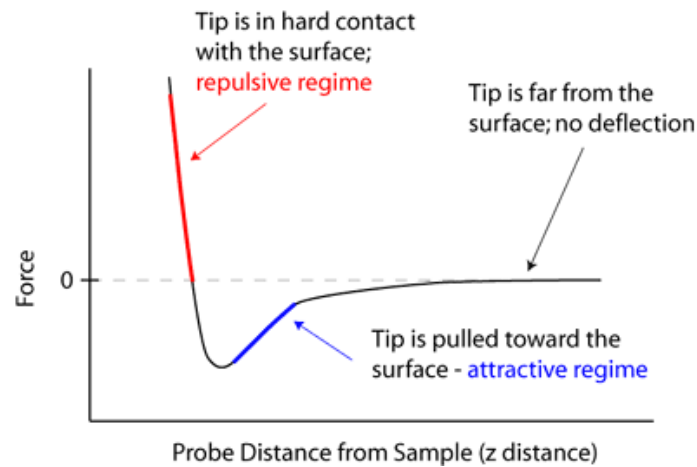
mode, the tip is only a few angstroms from the sample surface and the force
between the tip and the surface is kept constant during scanning by maintaining a
constant deflection, and therefore constant height above the surface. Since the tip is
in contact with the sample, a large lateral force is generated that can result in
damage to soft samples or cause movement of loosely attached objects.

To overcome this drawback, the second mode of operation is known as tapping
mode. In tapping mode, the problem of having high-lateral forces between the
cantilever and surface is eliminated by having the tip touch the surface for a very
short amount of time. To accomplish this, the cantilever is driven to oscillate up
and down near its resonance frequency by a small piezoelectric element mounted in
the AFM tip holder. The oscillating tip is then moved toward the surface until it
begins to lightly touch, or tap the surface. During scanning, the vertically
oscillating tip alternately contacts the surface and lifts off, generally at a frequency
of 50,000 to 500,000 cycles per second.[23] To gather information about the sample's
surface when in tapping mode, the amplitude of oscillation is maintained by a
feedback loop. If the tip approaches a bump in the surface, there is less room for

oscillation and thus, the amplitude decreases. If the tip approaches a depression on the sample's surface, there is more room for oscillation and the amplitude increases. When the digital feedback loop senses these changes in the oscillation amplitude, it can then adjusts the tip-sample separation to maintain a constant amplitude and force on the sample.[23]

For this research, a Veeco Dimension 3100 AFM was used to analyze the surface topography of the samples by performing scans of 1×1, 3×3, and 5×5 μm^2 for each sample. Due to there being a fixed number of pixels per scan line, the smaller area scans have better resolution and were used to analyze the fine details of the silicon nanoparticles while the larger area scans were used to look for long range patterns.

3.5.1   AFM Tip Profile

Another concern when working with AFM is the shape and material of the tip that is being used since these factors will have a direct effect on the resulting scans. This is an inherent feature of AFM and can never be fully removed. Any AFM image is a convolution of the shape of the probe, and the shape of the sample. This has the effect of making protruding features appear wide, and holes appear smaller (both narrower and often less deep, too). Broader (less sharp) probes will enhance the effect.[24] An example of this effect is shown in Figure 3.8.
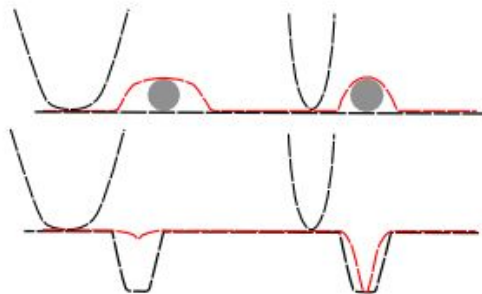

Figure 3.8: Effects of Tip Shape. This is an example of the convolution of the tip shape and sample.

For this research, a μmasch brand HQ:NSC14/AL-BS tip was used with a typical tip radius of less than 8nm and a full tip cone angle of 40°. It is made from n-type silicon with a bulk resistivity of 0.01 - 0.025 Ohm*cm and a total tip height of 12 - 18 μm. The typical resonant frequency is 160 kHz with force constant of 5 N/m. An image of the tip is shown in Figure 3.9 and a schematic of the cantilever is shown in Figure 3.10.
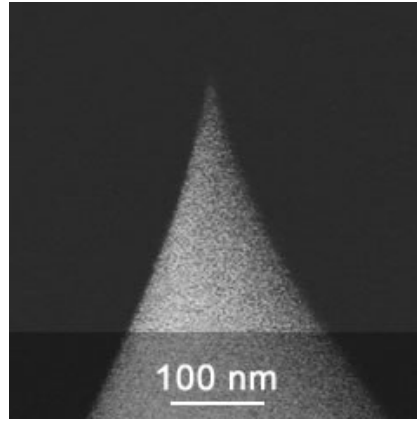

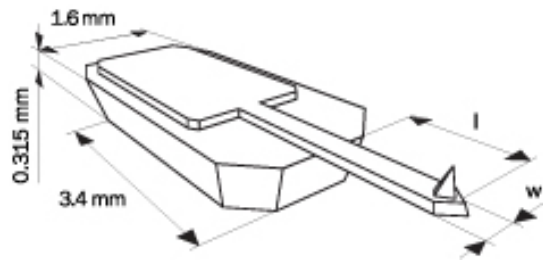Figure 3.9: SEM Image of AFM Tip. Close SEM up picture of the μmasch HQ:NSC14/AL-BS tip.

Figure 3.10: Schematic of AFM Tip. Schematic of the μmasch HQ:NSC14/AL-BS cantilever.

CHAPTER 4

EXPERIENTIAL PROCEDURE

In this chapter, I discuss the process used to clean the sample both before and after putting the substrate into the UHV system. Also the silicon deposition process and the method used to anneal our samples is described.

4.1 Substrate

The substrate used for this research was donated from Spansion's Fab 25 located in Austin, Texas and was a P type, boron doped silicon wafer with a thickness of 500-550μm. The wafer had a (1 0 0) orientation and resistivity of 10-20 ohm-cm. Fab 25 then grew a 400nm thick layer of SiO_2 using a Chemical Vapor Deposition (CVD) process.

4.2 Sample Preparation and Si Deposition

Before any deposition, the substrate was first cleaned by submerging the substrate in acetone and placing it in an Aquasonic Model 250D sonicator for 10 minutes followed by another 10 minute cycle in the sonicator with isopropyl alcohol. The sample was then rinsed with deionized water and blown dry using nitrogen gas. Following this initial cleaning, the sample was placed inside an AJA International ATC Orion Magnetron Sputtering System. Once the chamber had reached it's base pressure of around 5×10^{-8} torr, the cleaning was continued using RF Bias cleaning for 20 minutes at 25% power (12.5 watts) with an argon flow of 45 sccm to remove

any remaining contaminates from the surface of the substrate. To investigate the effect that this cleaning had on the original SiO2 thickness, we measured the oxide thickness before and after RF cleaning by ellipsometry for a control sample The measurement data was fit to a model consisting of Si(Si-JAW(bulk)) /SiO2mix(INT-JAW (1 nm)) /SiO2(SIO2-JAW, d nm) to estimate the SiO2 film thickness d. The oxide thickness decreased from 420 nm to 416 nm after the RF cleaning procedure. This accounts for a thickness decrease of less than 1%.

Once the RF Bias cleaning was finished and the chamber returned to it's base pressure, the silicon deposition could began. To ensure that the silicon target was free from contaminants, the silicon target was pre-sputtered with the shutter closed for 8 minutes at 20% power (60 watts) with an argon flow rate of 23 sccm at a working pressure of 1.2×10^{-3} torr. Once the pre-sputtering was finished, we could then open the silicon shutter and begin depositing the silicon layer. The parameters of the silicon deposition are summarized in Table 4.1.

Table 4.1: Silicon Deposition Parameters.

Base Pressure	5×10^{-8} torr
Working Pressure	1.2×10^{-3} torr
Argon Gas Flow Rate	23 sccm
RF Power	60 watts
Pre-Sputter Duration	5 minutes

From earlier testing using a Maxtek Model TM-350/400 Thickness Monitor installed in the AJA Sputtering System, we found the rate of silicon deposition at 20% power with an argon flow of 23 sccm is about 8.8 Å/minute. The data used to determine this rate is shown in Table 4.2.

The deposition rate calculated by the film thickness monitor was used to create sets of samples with expected silicon layer thicknesses of 5, 10, and 15 nm. The deposited samples were analyzed by ellipsometry. The following model was used to determine the thickness (d) of the silicon layer: Silicon-wafer/SiO2-Si mix(1

Table 4.2: Silicon Deposition Rate. Silicon deposition rate at 20% power as measured by the film thickness monitor.

Time	Rate
1 Min	0.016kÅ
2 Min	0.025kÅ
3 Min	0.032kÅ
4 Min	0.038kÅ
5 Min	0.044kÅ
Rate	8.8 Å/min

Table 4.3: Corrected Silicon Layer Thicknesses. Expected silicon layer thicknesses based on the film thickness monitor deposition rate and the actual silicon layer thickness based on spectroscopy results.

Expected Thickness	Deposition Time	Actual Thickness
5 nm	5 min 41 sec	3.07 nm
10 nm	11 min 22 sec	6.20 nm
15 nm	17 min 1 sec	9.30 nm

nm)/amorphous Si-crystalline-Si EMA (d nm). The thicknesses determined by ellipsometry were approximately 62% of the values determined with the thickness monitor. It is not clear why the deposition rate of the thickness monitor was off. The corrected thickness data is summarized in Table 4.3.

4.3   Rapid Thermal Annealing

We annealed our samples using a Heatpulse 610 Rapid Thermal Processing System that heated the sample via high intensity tungsten-halogen lamps in an argon environment at atmospheric pressure. This rapid thermal annealing system can increase the temperature at a maximum rate of 200°C per second and can reach a maximum temperature of 1100°C. For our samples, the temperatures used ranged

from 600 - 800°C increasing at a rate of 150°C per second and were held at the high temperature between 30 and 120 seconds.

Two groups of samples were created for this study. The first group was created to observe nanoparticle formation as a function of silicon top layer thickness and annealing temperature. For this group, a sample from each of the silicon top layer thicknesses (3, 6, and 9 nm) were annealed at 600, 700, and 800°C for 60 seconds. The second group was created to observe nanoparticle formation as a function of annealing duration. For this group, samples with a silicon top layer thickness of 9 nm were annealed at 700°C for 30, 60, 90, and 120 seconds.

The main advantages of using RTA are that we could reach the higher nanoparticle formation temperatures that were reported by previous studies, as well as the ability to bring the sample to the annealing temperature very quickly.[5,9]

There are a few disadvantages to this method as well. The main disadvantage is the fact that oxidation is a very real possibility. In order to use the rapid thermal annealer, we must take the silicon deposited sample out of the UHV and place it in the RTA. Once the sample is in the RTA, we start to flow ultra-high purity argon into the system at a rate of approximately 5 liters per minute. It is during this transition period when the deposited silicon could form a native oxide which could lead to increasing the temperature of nanoparticle formation by as much as 50°C.[9]

4.3.1 Optical Analysis

After annealing, samples were allowed to cool before any further analysis could take place. Once the temperatures of the samples were below 80°C, they were taken out of the argon environment and then examined using the spectroscopic ellipsometer. Efforts were made to minimize the amount of time that the samples were exposed to air to try to reduce further oxidation. Using the variable angle spectroscopic ellipsometer, the samples were analyzed using wavelengths of 0.27

µm to 0.9 µm and at angles of incidents of 55, 60, 65, 70, and 75 degrees.

4.3.2   AFM Analysis

After optical data was gathered for the samples, the surface topography of the sample were then analyzed using an AFM. For each sample, scans were made of 1x1 µm , 3x3 µm , and 5x5 µm to observe nanoparticle formation. Due to there being a fixed number of pixels per scan line, the smaller area scans have better resolution and were used to analyze the fine details of the silicon nanoparticles while the larger area scans were used to look for long range patterns.

CHAPTER 5

DATA AND ANALYSIS

In this chapter, the results of the AFM and VASE analysis will be presented. First, the AFM characterization is presented along with the nanoparticle size and distribution. Second, the results of the VASE data and the model used to represent the samples will be discussed.

5.1 Unannealed and Annealed SiO$_2$ Control Samples

Control samples were used to ensure that the observed nanoparticle formation was in fact due to annealing a thin film of silicon and not caused by annealing the silicon dioxide layer. These control samples were cleaved from the same substrate used by the nanoparticle samples and consisted solely of a SiO$_2$ layer approximately 420 nm thick on top of a silicon (100) substrate. The control sample was subjected to the same cleaning and annealing process used by the nanoparticle samples and was analyzed using an AFM after cleaning and after annealing. The control sample was annealed at 700°C for 60 second. The results of the AFM analysis is shown in Figure 5.1.

The AFM analysis of the SiO$_2$ both before and after annealing show that the surface remains relatively smooth with only a small increase in the roughness and that there is no nanoparticle formation in the absence of the silicon layer. The RMS roughness of the unannealed SiO$_2$ layer is 0.197 nm and 0.233 nm for the annealed SiO$_2$ layer.

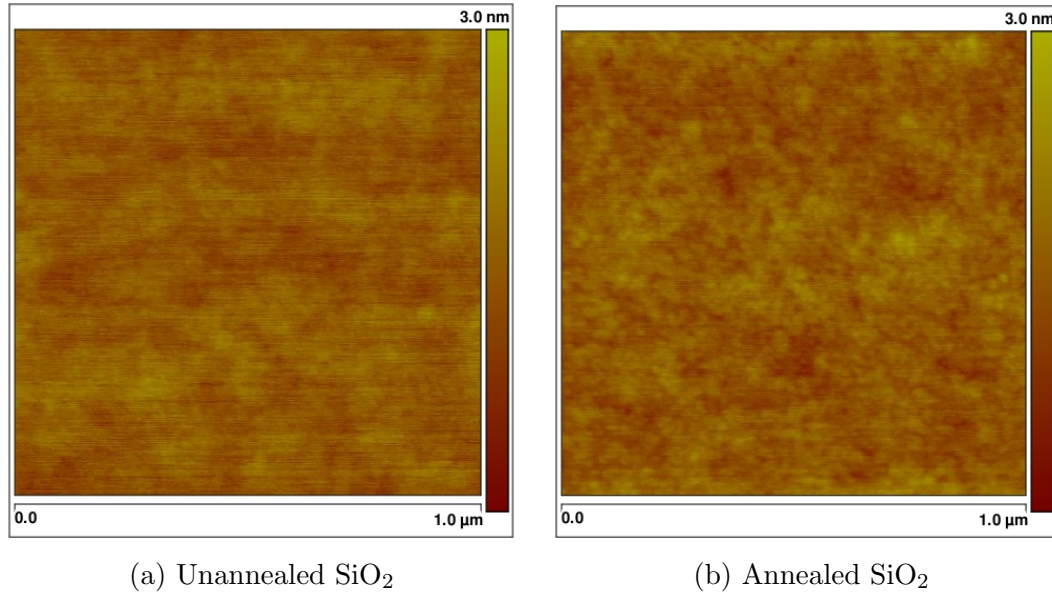(a) Unannealed SiO$_2$ (b) Annealed SiO$_2$

Figure 5.1: AFM Images of Control Samples. AFM image of the unannealed SiO$_2$ oxide layer (left) and the annealed SiO$_2$ oxide layer (right). Both images are scans of 1 x 1 μm^2.

5.2 AFM Analysis of Nanoparticles as a Function of Layer Thickness and Annealing Temperature

To analyze the nanoparticle size and distribution as a function of silicon top layer thickness and annealing temperature, three groups of samples were created with silicon top layer thicknesses of 3, 6, and 9 nm. For each silicon layer thickness, samples were annealed at 600, 700, and 800°C for 60 seconds each. Three AFM images were taken at each temperature and for each silicon layer thickness with scan sizes of 1 x 1, 3 x 3, and 5 x 5 μm^2. The results of these scans are shown in Figures 5.4 - 5.12.

Two methods were used to determine the size and distribution of the created nanoparticles. The first method to be discussed will be referred to as the threshold method and involved using the MATLAB function `imextendedmax` to identify all regional maxima that are greater than or less than a specified threshold. The second method, referred to as the peak-to-peak method, used a process in which a peak was

chosen at random and the distance to the next closest peak was calculated.

Both methods first involved converting 1 x 1µm² AFM images into TIFF files which were then loaded into MATLAB. Once in MATLAB, the images were stored as a 512 by 512 matrix. Each element in this matrix was an integer ranging from 0 to 255 which corresponded to the AFM height at each pixel. An example of what a small image matrix would look like is shown in Figure 5.2.

```
A = [10    10    10    10    10    10    10    10    10    10;
     10    13    13    13    10    10    11    10    11    10;
     10    13    13    13    10    10    10    11    10    10;
     10    13    13    13    10    10    11    10    11    10;
     10    10    10    10    10    10    10    10    10    10;
     10    11    10    10    10    18    18    18    10    10;
     10    10    10    11    10    18    18    18    10    10;
     10    10    11    10    10    18    18    18    10    10;
     10    11    10    11    10    10    10    10    10    10;
     10    10    10    10    10    10    11    10    10    10]
```

Figure 5.2: Example of an Image Matrix in MATLAB. In the matrix, the grey high-lighted regions represent peaks in the image.

In the threshold method, peaks are identified by locating areas of the image where the change in intensity is extreme; that is, the difference between the pixel and neighboring pixels is greater than a certain threshold. For example, to find only those regional maxima in the matrix A of Figure 5.2 that are at least two units higher than their neighbors, the function `imextendedmax` would be used with a threshold of 2. The result of this operation is the binary matrix B shown in Figure 5.3. Identified peaks are converted to areas of ones while non-peak areas are converted to zeros.

The threshold value used to determine the peaks in each image was the standard deviation of the heights of the image. The diameter of the located peaks was calculated by using the resulting binary matrix and the `MajorAxisLength` property
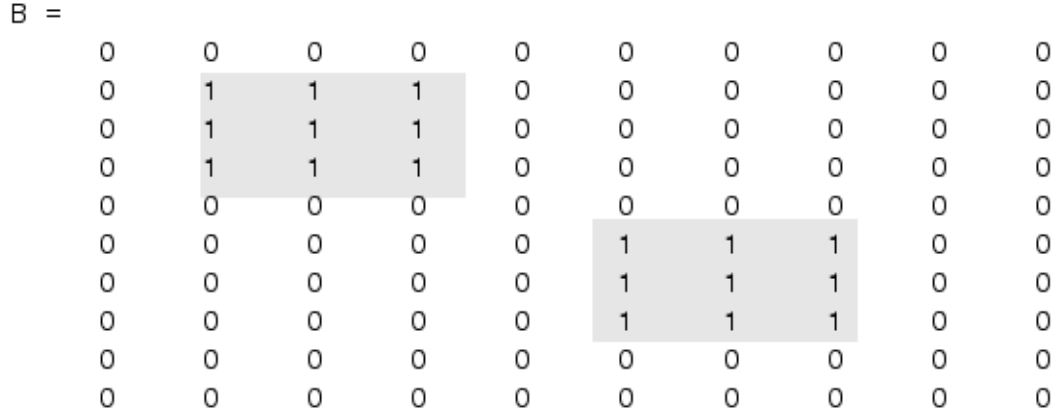
B =

0	0	0	0	0	0	0	0	0	0
0	1	1	1	0	0	0	0	0	0
0	1	1	1	0	0	0	0	0	0
0	1	1	1	0	0	0	0	0	0
0	0	0	0	0	0	0	0	0	0
0	0	0	0	0	1	1	1	0	0
0	0	0	0	0	1	1	1	0	0
0	0	0	0	0	1	1	1	0	0
0	0	0	0	0	0	0	0	0	0
0	0	0	0	0	0	0	0	0	0

Figure 5.3: Result of Imextendedmax. Peaks larger than the threshold value are converted to ones and all other elements are converted to zeros.

of MATLAB's Image Processing Toolbox. The `MajorAxisLength` property specifies the length (in pixels) of the major axis of the ellipse that is fitted to the region. Using this information along with the pixel resolution, the radius of the particles in nanometers could be calculated.

In the peak-to-peak method, 300 peaks were chosen at random for each 1 x 1μm^2 AFM image. For each peak chosen, the distance (in pixels) between the chosen peak and the next closet peak was calculated. It is assumed that this distance is the sum of the two equal radii of the particles. Therefore, dividing this distance by two and multiplying by the pixel resolution gives the radius of the particles.

In general, both the threshold method and the peak-to-peak method found very similar results for both nanoparticle size and distribution. However, it is useful to note that the distributions of the peak-to-peak method tended to be slightly more narrow than that of the threshold method. This is most likely attributed to the smaller fixed sample size of 300 peaks and the possibility of double counting in samples with fewer peaks overall. Due to these difficulties, the threshold method is the main method used to determine to particle size and distributions for this research with the peak-to-peak method being used as a double check.

5.2.1 AFM Analysis of 3 nm Si Layer Annealed for 60 Seconds

The following are AFM images of samples with a 3 nm amorphous silicon (α-Si) top layer that were annealed and 600, 700, and 800°C for 60 seconds. These anneals produced wide particles with a gradual slope.
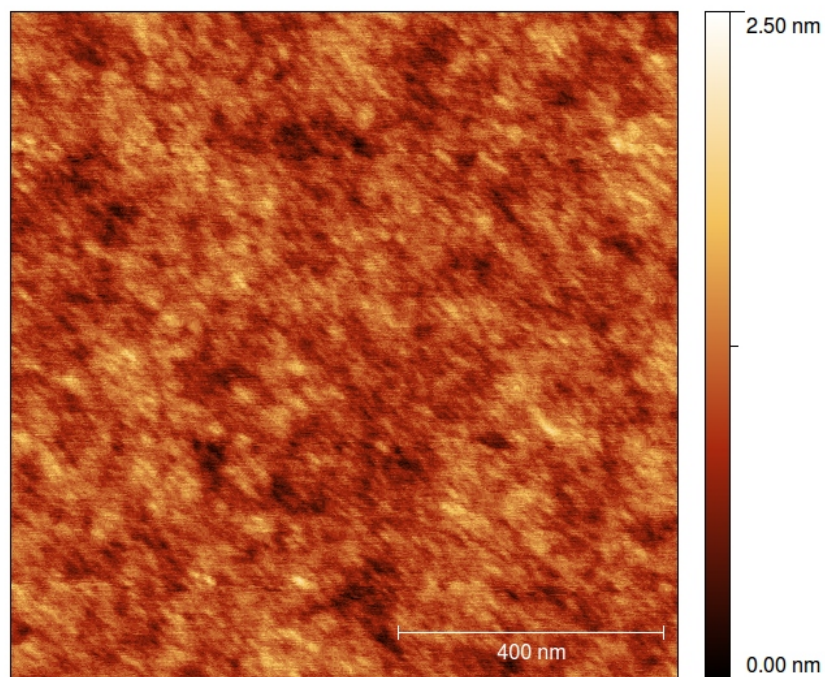

(a) 1 μm x 1 μm

(b) 3 μm x 3 μm
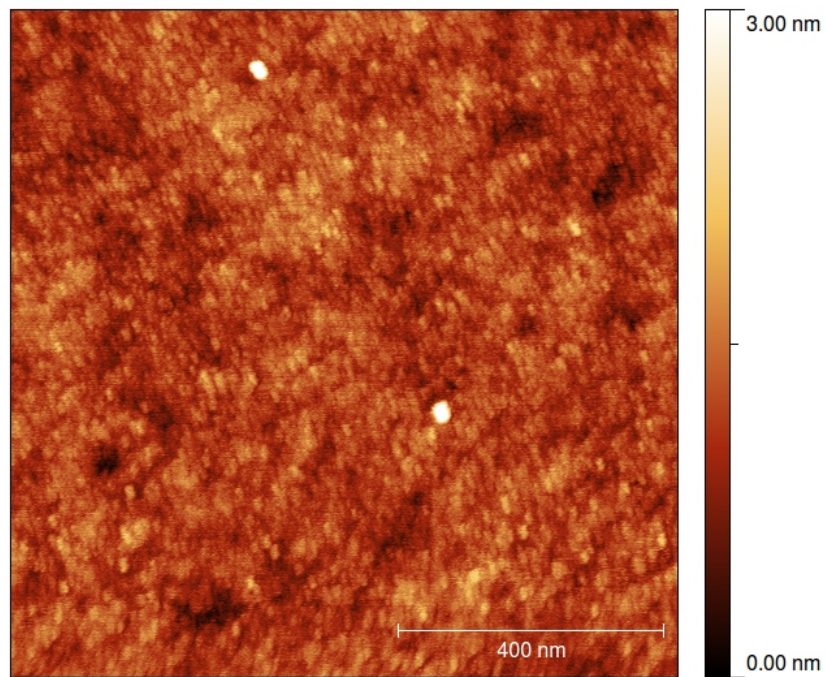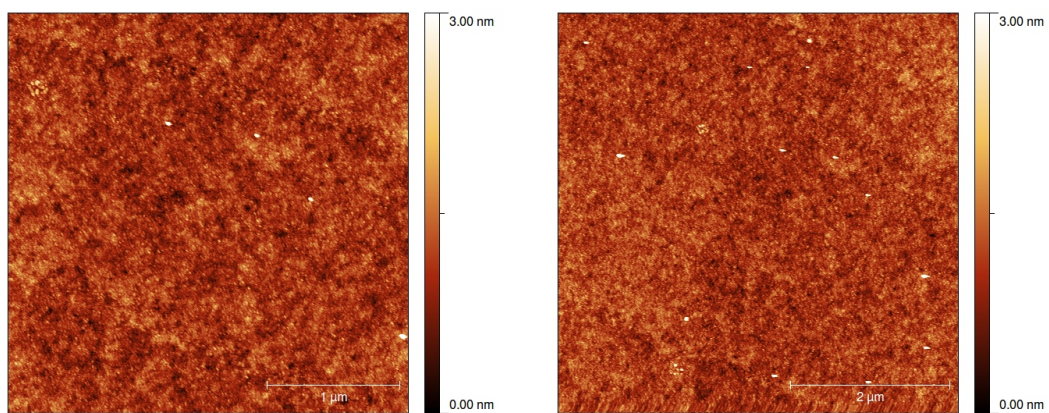
(c) 5 μm x 5 μm

Figure 5.4: 3 nm Si layer annealed at 600°C for 60 seconds.

(a) 1 μm x 1 μm

(b) 3 μm x 3 μm
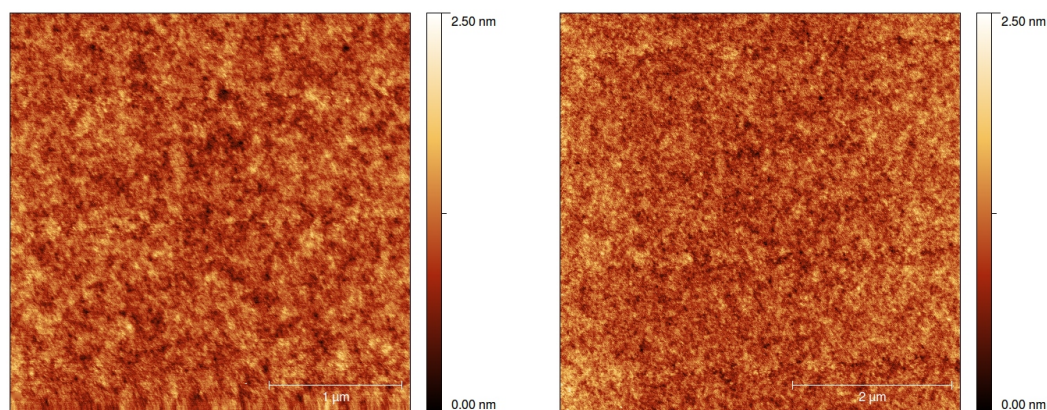
(c) 5 μm x 5 μm

Figure 5.5: 3 nm Si layer annealed at 700°C for 60 seconds.

(a) 1 μm x 1 μm

(b) 3 μm x 3 μm
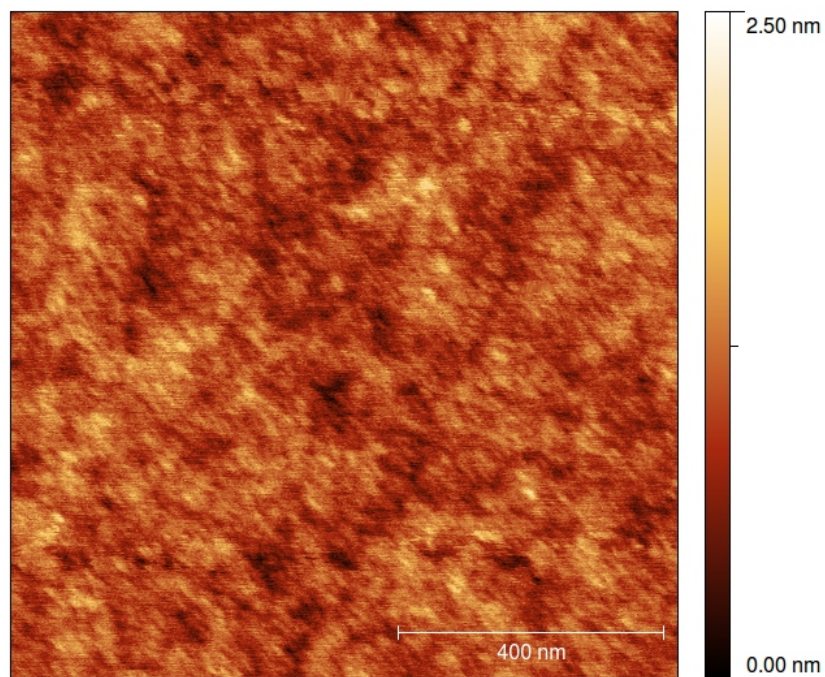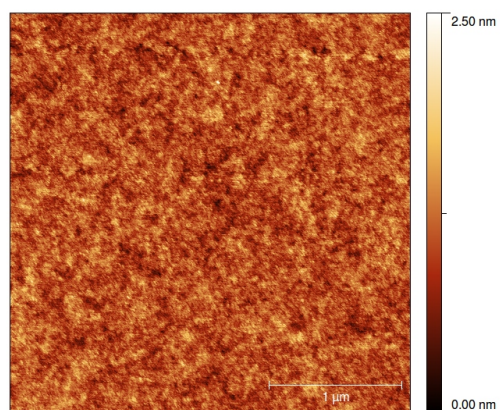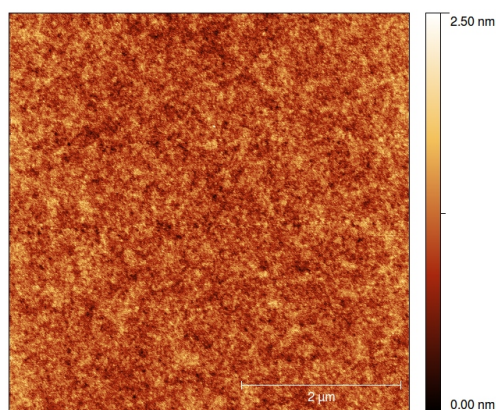
(c) 5 μm x 5 μm

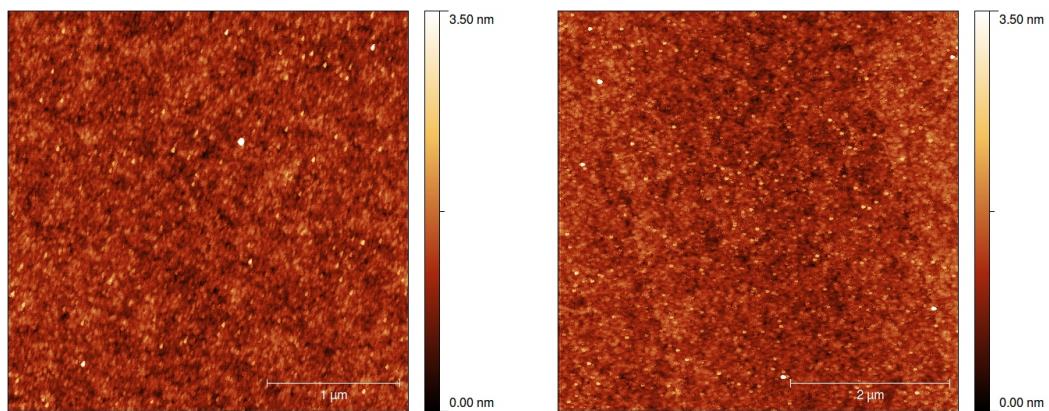Figure 5.6: 3 nm Si layer annealed at 800°C for 60 seconds.

5.2.2   AFM Analysis of 6 nm Si Layer Annealed for 60 Seconds

As the thickness of the α-Si layer increases, so does the shape of the formed particles. With a 6 nm layer of α-Si, the slope of the particles increases along with their height causing them to become more pronounced in the images below.
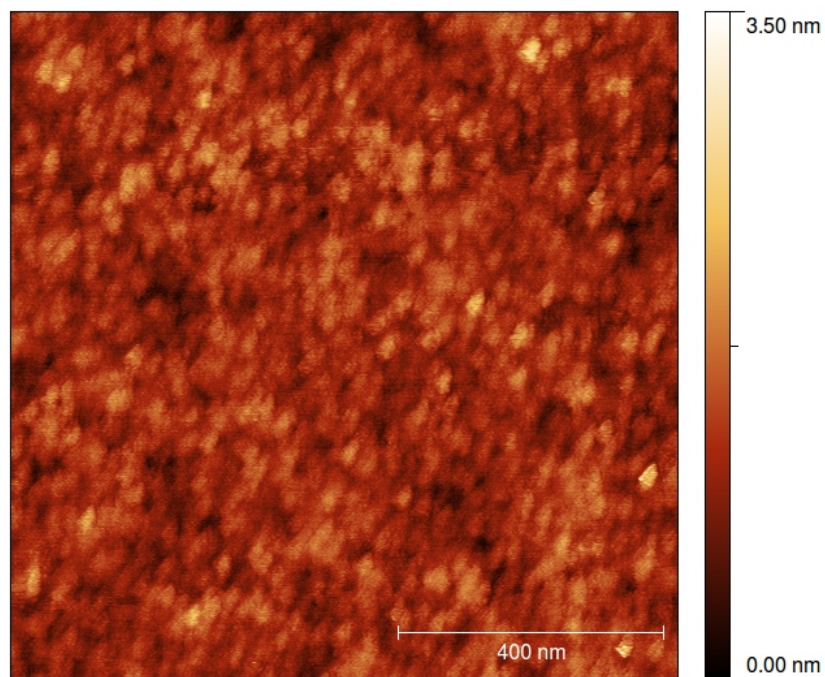

(a) 1 μm x 1 μm

(b) 3 μm x 3 μm
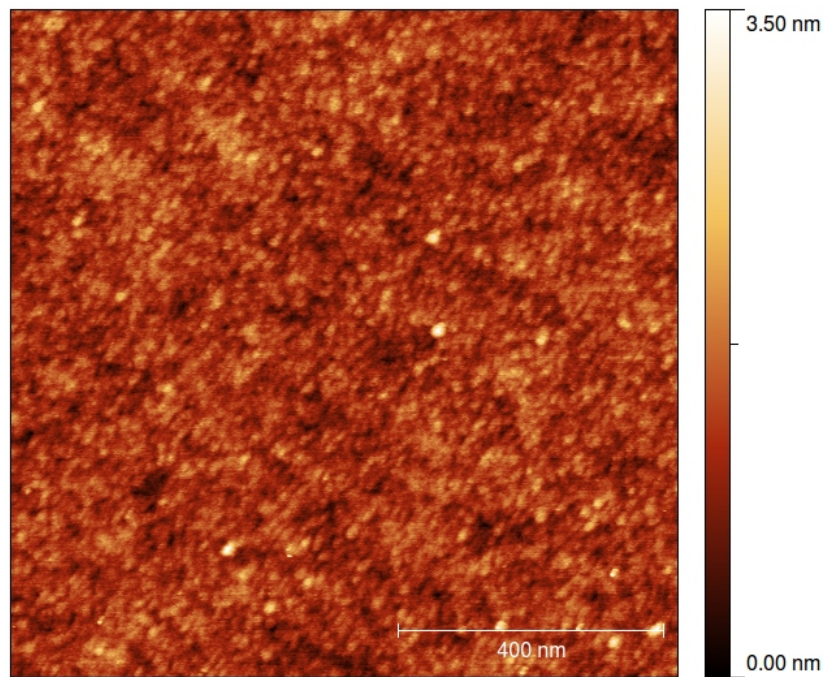
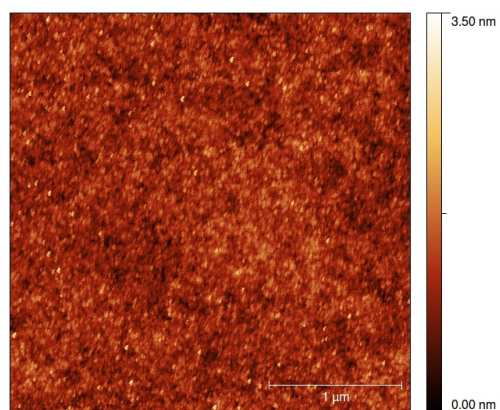(c) 5 μm x 5 μm

Figure 5.7: 6 nm Si layer annealed at 600°C for 60 seconds.

(a) 1 μm x 1 μm

(b) 3 μm x 3 μm
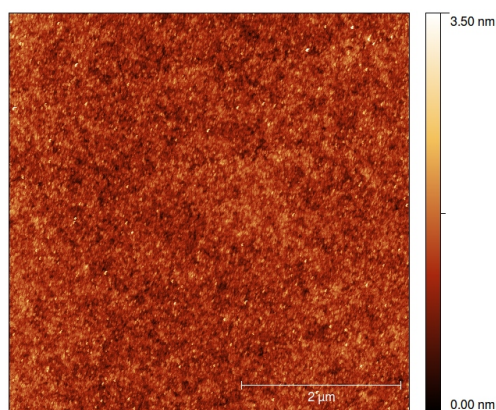
(c) 5 μm x 5 μm

Figure 5.8: 6 nm Si layer annealed at 700°C for 60 seconds.

(a) 1 μm x 1 μm

(b) 3 μm x 3 μm
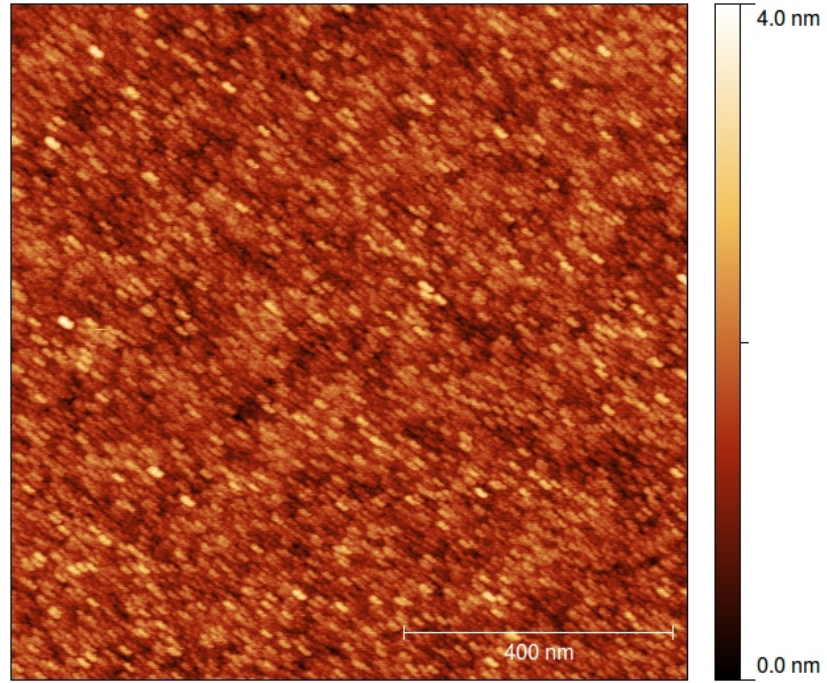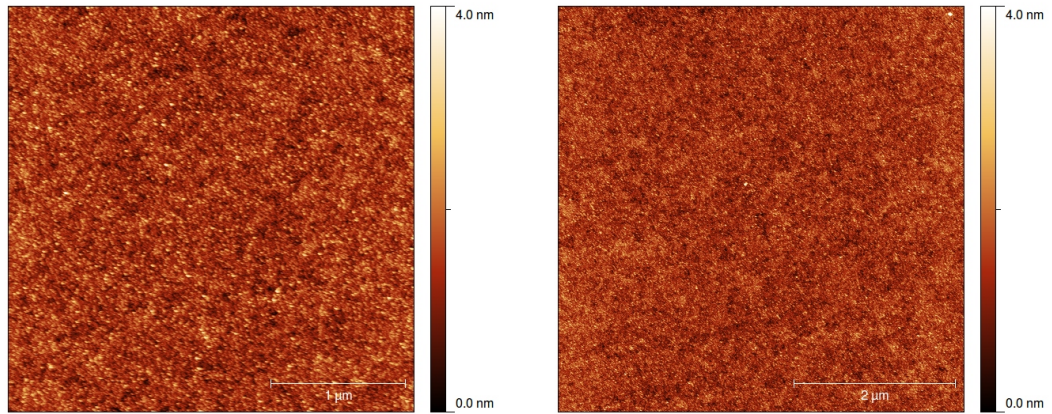
(c) 5 μm x 5 μm

Figure 5.9: 6 nm Si layer annealed at 800°C for 60 seconds.

5.2.3 AFM Analysis of 9 nm Si Layer Annealed for 60 Seconds

The formed particles become much more defined as the thickness of the α-Si layer is increased to 9 nm. These particles have a very steep slope as well as smaller and more uniform radii than particles of thinner silicon layers.

(a) 1 μm x 1 μm

(b) 3 μm x 3 μm
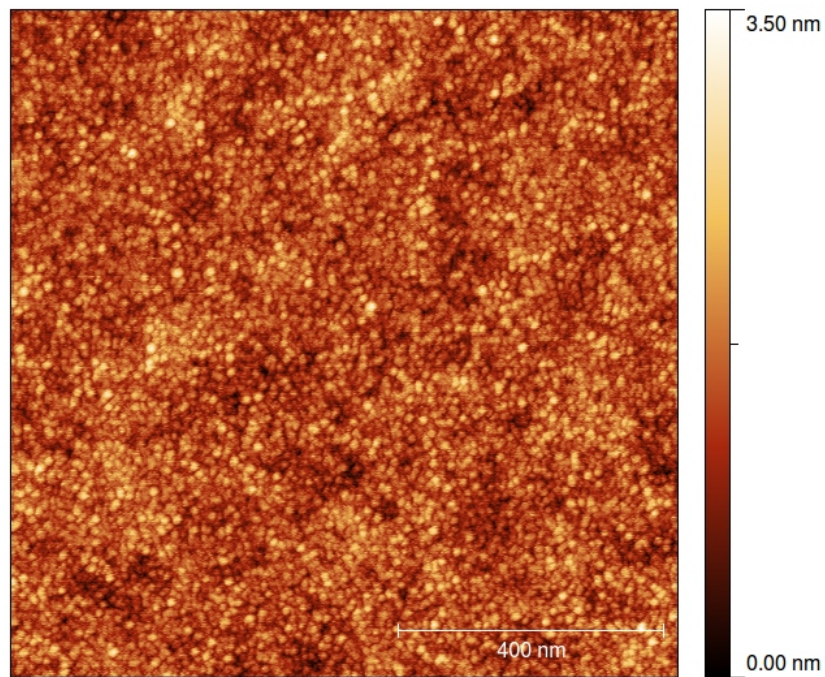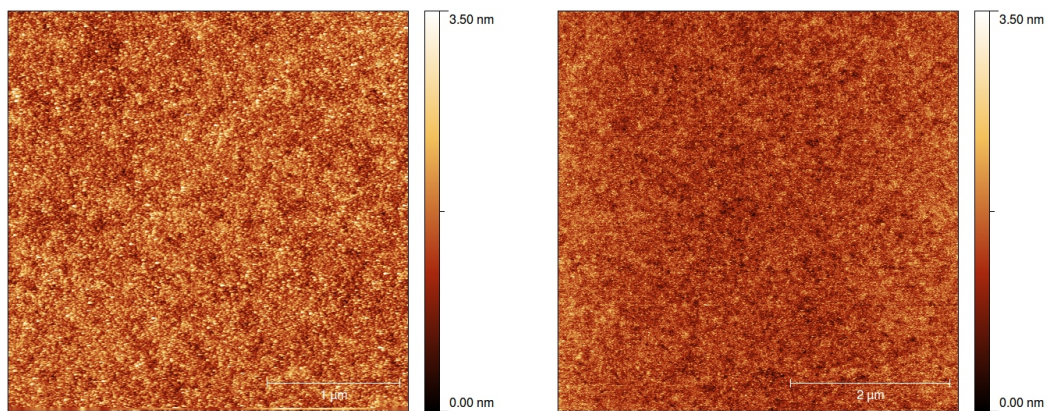
(c) 5 μm x 5 μm

Figure 5.10: 9 nm Si layer annealed at 600°C for 60 seconds.

(a) 1 μm x 1 μm

(b) 3 μm x 3 μm
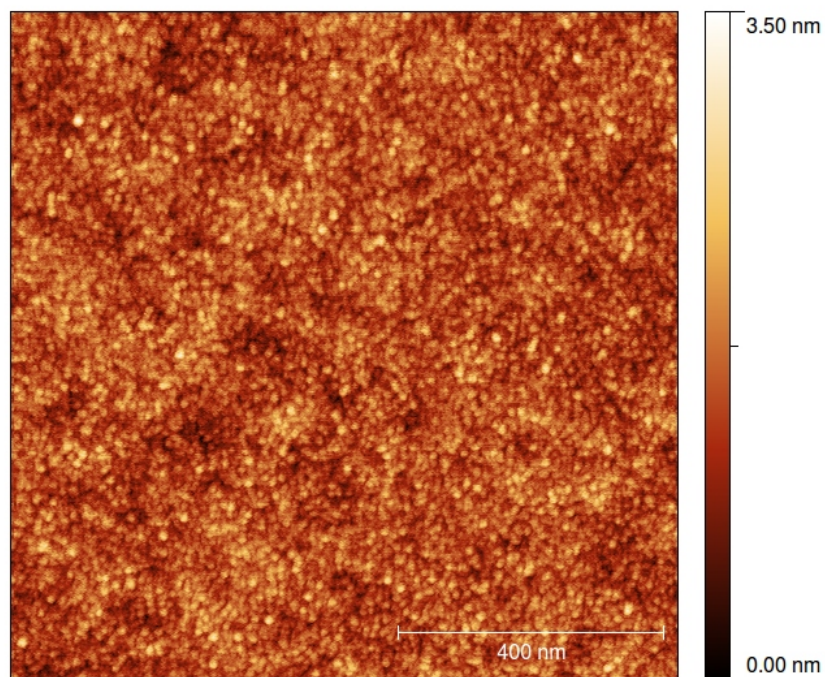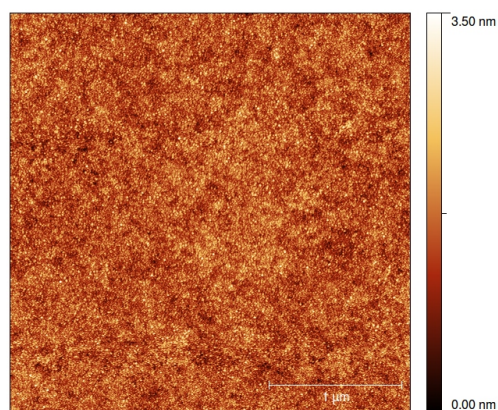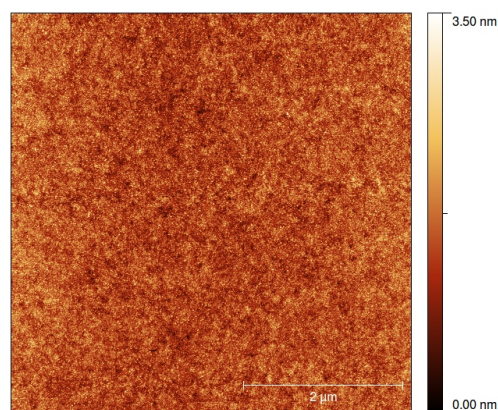
(c) 5 μm x 5 μm

Figure 5.11: 9 nm Si layer annealed at 700°C for 60 seconds.

(a) 1 μm x 1 μm

(b) 3 μm x 3 μm
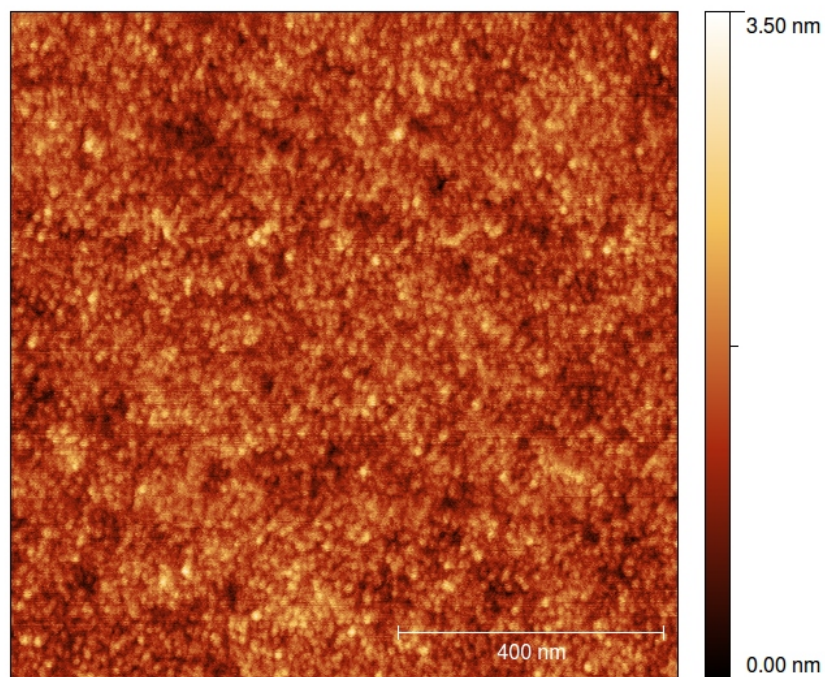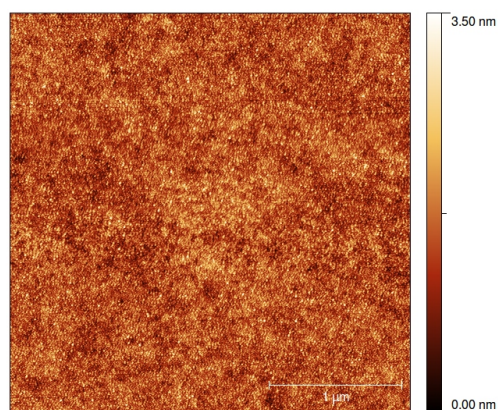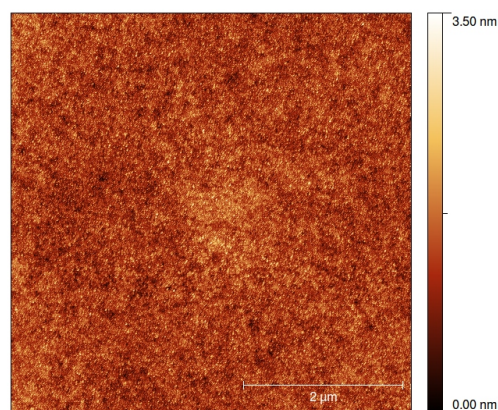
(c) 5 μm x 5 μm

Figure 5.12: 9 nm Si layer annealed at 800°C for 60 seconds.

It is obvious from the AFM images that the size of the nanoparticles change as a function of silicon top layer thickness and annealing temperature. To better illustrate this, Figure 5.13 and Figure 5.14 show the nanoparticle distribution for all of the silicon top layer thickness as well as for all of the annealing temperatures. When viewed in this fashion, trends in size of the nanoparticle start to appear. The first trend is that as the thickness of the silicon top layer increases, the distribution of nanoparticle size becomes much more narrow. The second trend is that as the annealing temperature increases, so do the average nanoparticle size. Table 5.1 shows the average nanoparticle radius for each for each of the silicon top layer thicknesses and annealing temperature calculated by the threshold method. Table 5.2 shows the average radius as calculated by the peak-to-peak method. Both methods yield similar results.

Table 5.1: Nanoparticle Radius using Threshold Method. Average Nanoparticle radius versus silicon thickness and annealing temperature calculated using the threshold method.

	600°C	700°C	800°C
3 nm	7.65 nm	9.91 nm	8.78 nm
6 nm	8.19 nm	8.93 nm	9.03 nm
9 nm	5.97 nm	6.28 nm	6.47 nm

Table 5.2: Nanoparticle Radius using Peak-to-Peak Method. Average Nanoparticle radius versus silicon thickness and annealing temperature calculated using the peak-to-peak method.

	600°C	700°C	800°C
3 nm	8.67 nm	9.28 nm	8.84 nm
6 nm	8.43 nm	9.58 nm	8.66 nm
9 nm	6.84 nm	7.29 nm	7.78 nm

To better understand the broad distribution of the 3 and 6 nm silicon layer samples as compared to the narrow distribution of the 9 nm samples, a line profile of the nanoparticles as measured by AFM is shown in Figure 5.15. In this figure, the
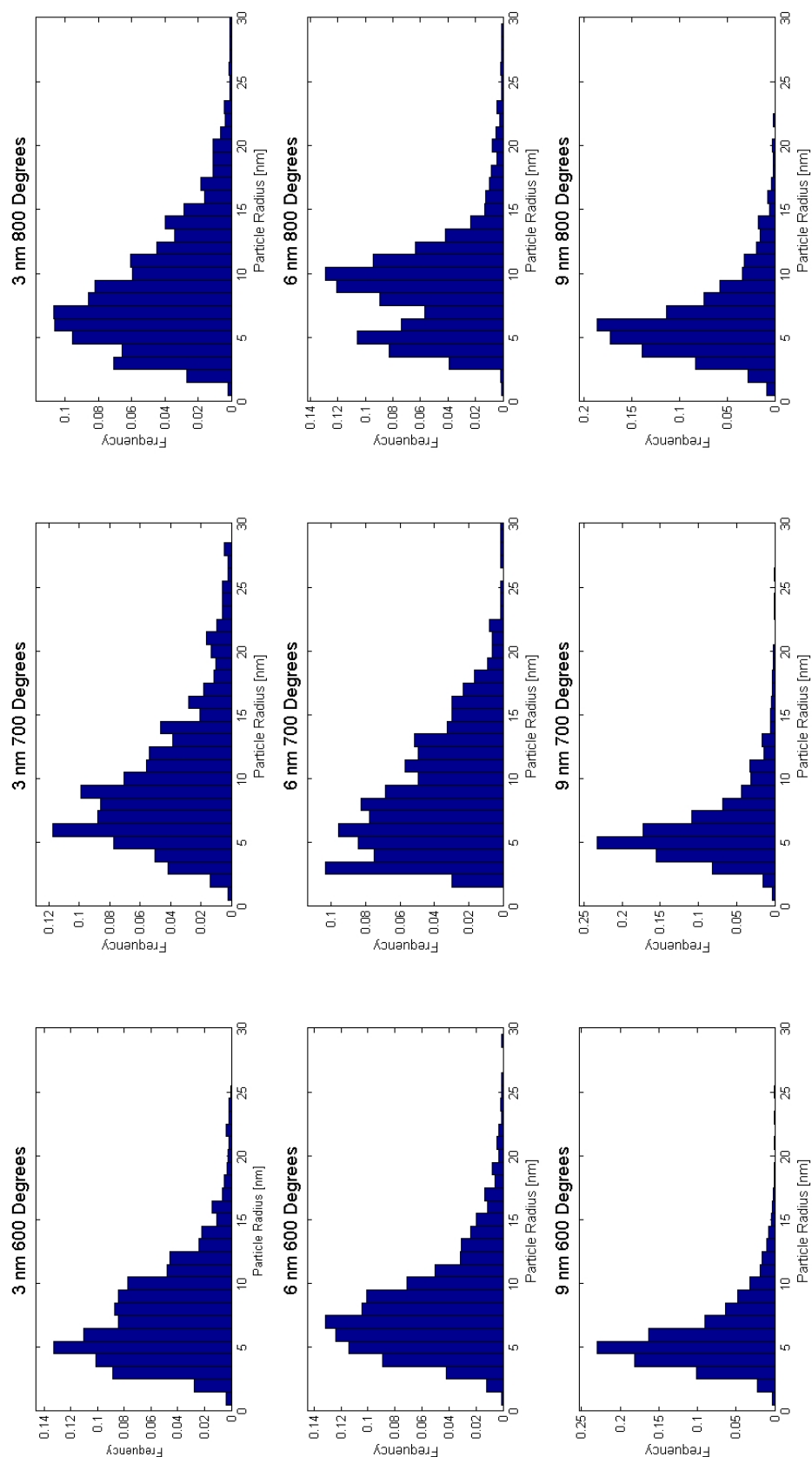
Figure 5.13: Nanoparticle Distributions by Threshold Method. Size distributions for each silicon top layer thickness and annealing temperature.
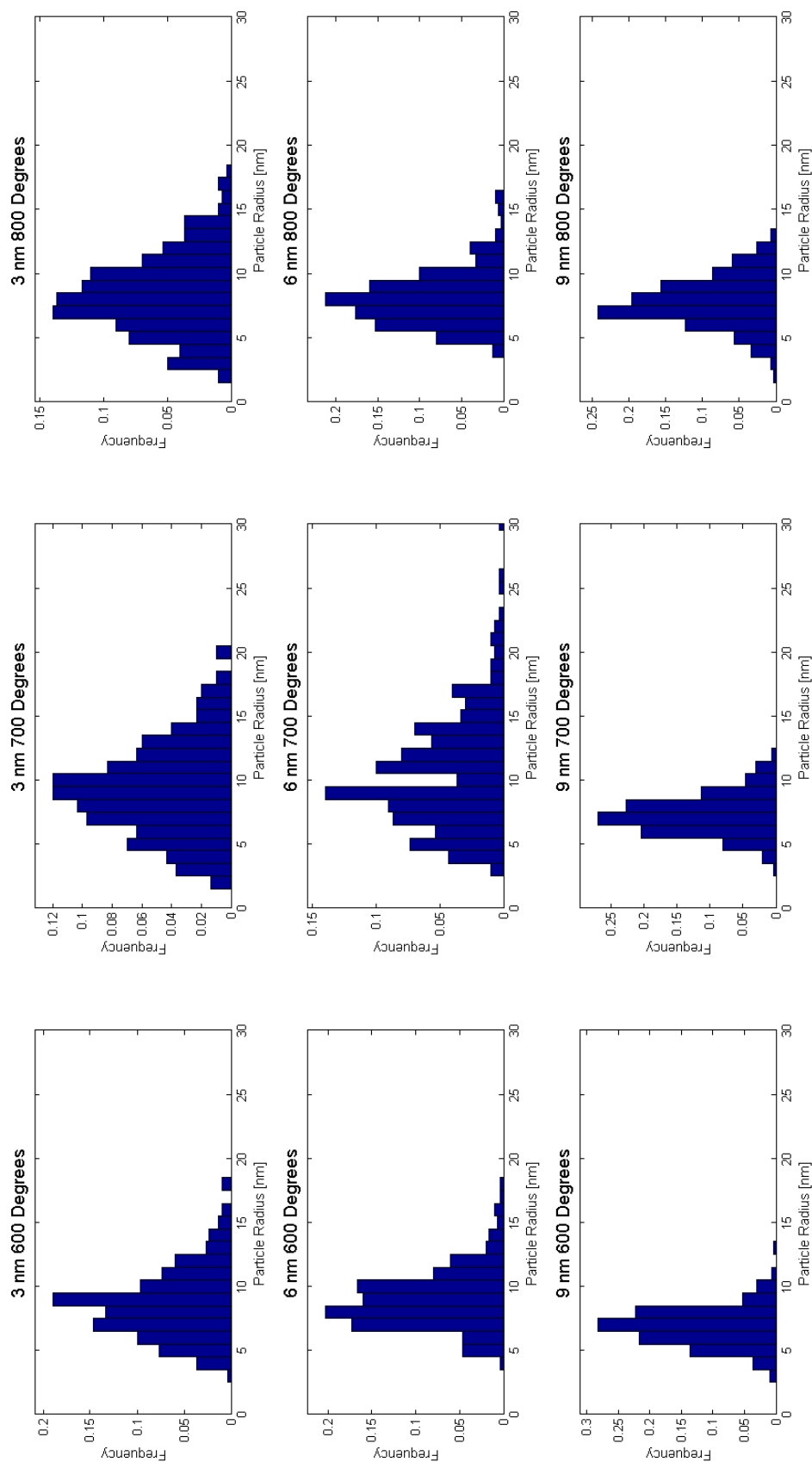
Figure 5.14: Nanoparticle Distributions by Peak-to-Peak Method. Size distributions for each silicon top layer thickness and annealing temperature.
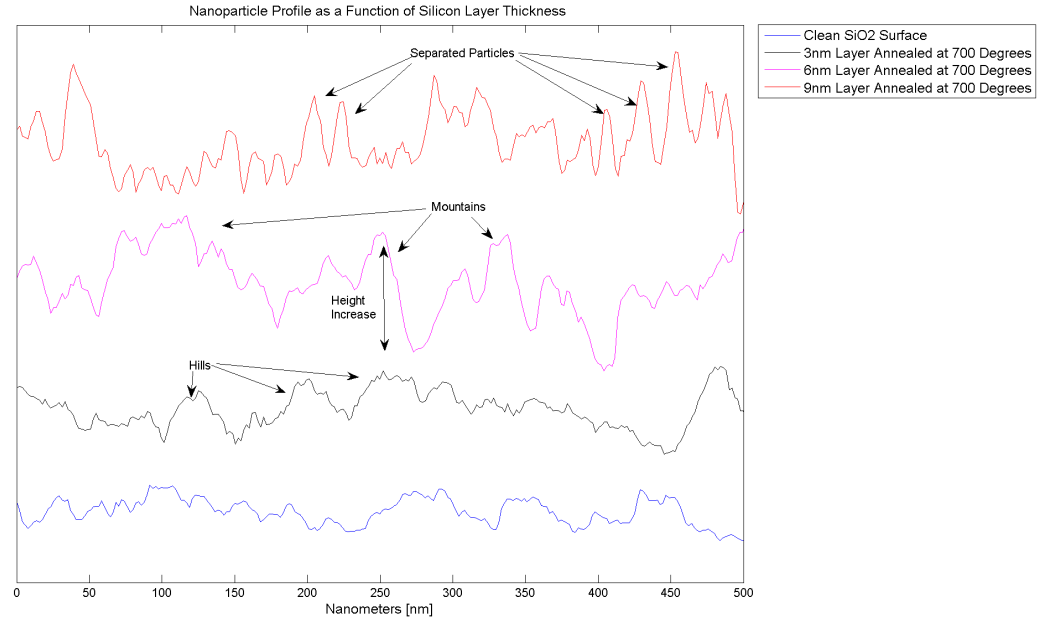
Figure 5.15: Profile of Nanoparticles. Profile of silicon nanoparticles as a function of initial silicon layer thickness.

profile of the cleaned SiO_2 sample is compared to that of samples that have 3, 6, and 9 nm layers of silicon that were annealed at 700°C for 60 seconds. As the thickness of the silicon increases, a pattern starts to emerge. After annealing, the surface of the 3 nm silicon layer starts to form rather large hills. As the thickness increases to 6 nm, these hills become more profound and their height increases turning more into mountain than hills. Once the silicon is 9 nm thick, these mountains start to separate and form narrow and well defined nanoparticles. This gradual change from hills to steep nanoparticles helps to explain why the MATLAB algorithm calculated particles of a larger radius and distribution for the thinner silicon layer and smaller radius and much more narrow distribution for the thicker silicon layers.

For the most part, silicon nanoparticles formed during this research are smaller than the nanoparticles of previous work, however there are some similarities. In the work completed by B. Legrand *et al.*,[9] many samples exhibited a bimodal distributions of nanoparticle sizes. In their work, nanoparticle radius distribution

peaks were observed at 9 and 45 nm for a silicon top layer of 3 nm and at 10 and 60 nm for a 6 nm silicon top layer. In this work, the mean nanoparticle radii found for the 3 and 6 nm silicon layer thickness match closely to the smaller particle radii observed by Legand's work.

5.3   AFM Analysis of Nanoparticle Formation as a Function of Annealing Duration

For this research, nanoparticle size and distribution were also analyzed as a function of annealing duration. To accomplish this, samples with a 9 nm silicon top layer were annealed at 700°C for 30, 60, 90, and 120 seconds. Three images were taken of each sample with scan sizes of 1 x 1, 3 x 3, and 5 x 5 μm^2 and are shown in Figures 5.16-5.19. These samples were also analyzed using MATLAB to determine the nanoparticle distributions.

5.3.1 AFM Analysis of 9 nm Si Layer Annealed for 30 Seconds

This is a 9 nm α-Si layer that was annealed at 700°C for 30 seconds.

(a) 1 μm x 1 μm

(b) 3 μm x 3 μm
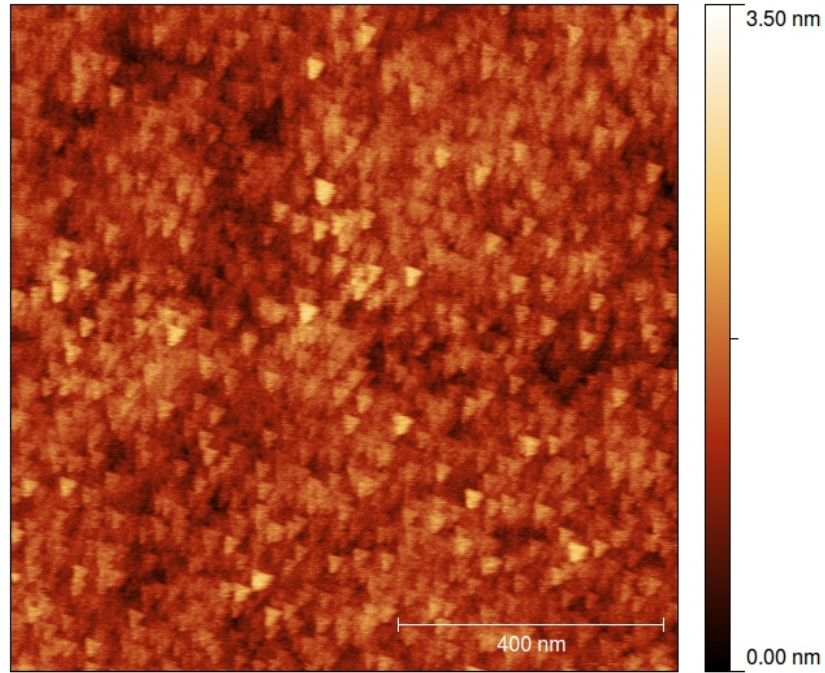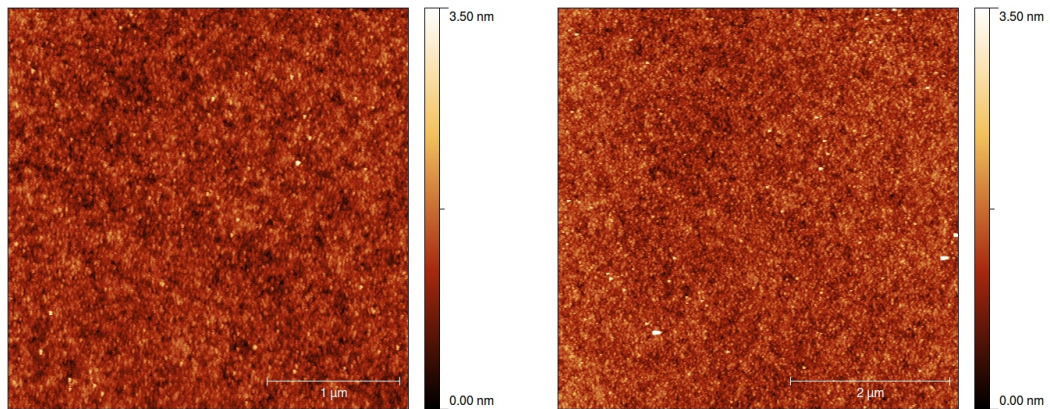
(c) 5 μm x 5 μm

Figure 5.16: 9 nm Si layer annealed at 700°C for 30 seconds.

5.3.2 AFM Analysis of 9 nm Si Layer Annealed for 60 Seconds

This is a 9 nm α-Si layer that was annealed at 700°C for 60 seconds.

(a) 1 μm x 1 μm

(b) 3 μm x 3 μm

(c) 5 μm x 5 μm

Figure 5.17: 9 nm Si layer annealed at 700°C for 60 seconds.

5.3.3 AFM Analysis of 9 nm Si Layer Annealed for 90 Seconds

This is a 9 nm α-Si layer that was annealed at 700°C for 90 seconds.

(a) 1 μm x 1 μm

(b) 3 μm x 3 μm
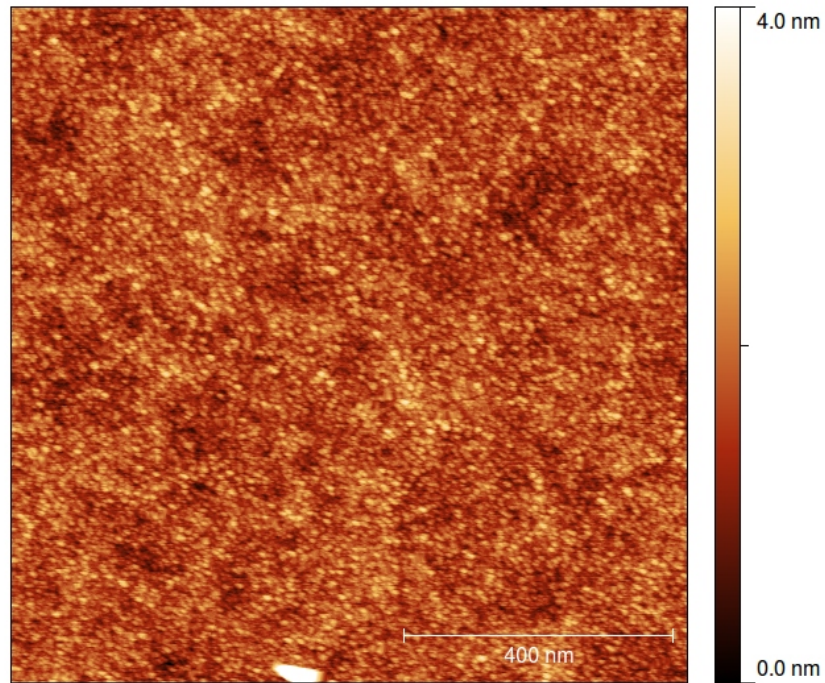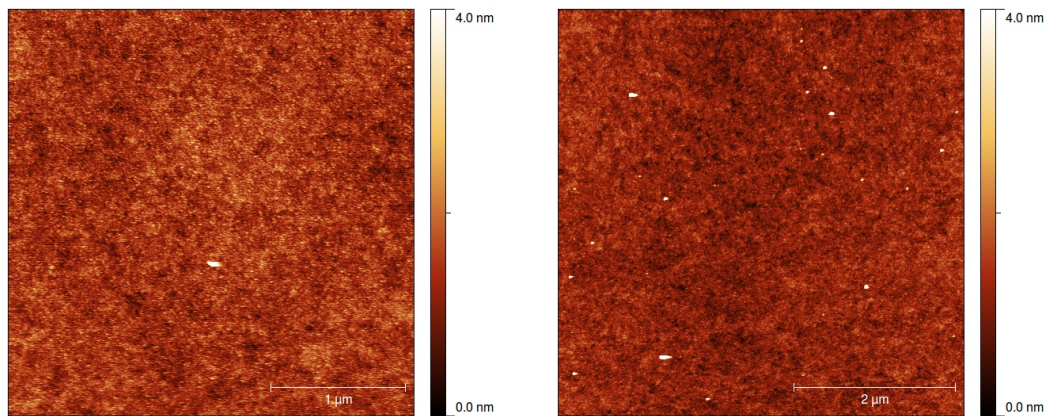
(c) 5 μm x 5 μm

Figure 5.18: 9 nm Si layer annealed at 700°C for 90 seconds.

5.3.4 AFM Analysis of 9 nm Si Layer Annealed for 120 Seconds

This is a 9 nm α-Si layer that was annealed at 700°C for 120 seconds.

(a) 1 μm x 1 μm

(b) 3 μm x 3 μm
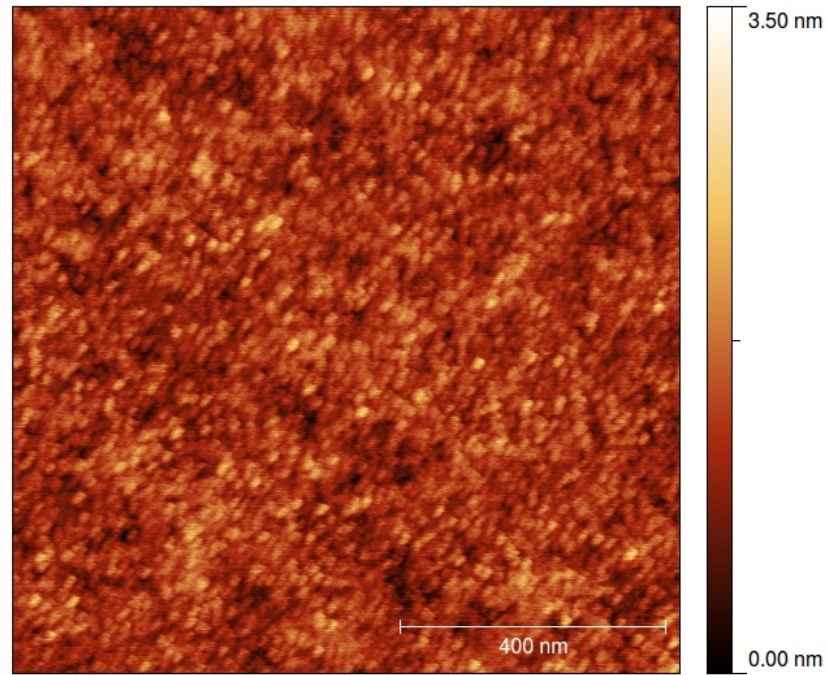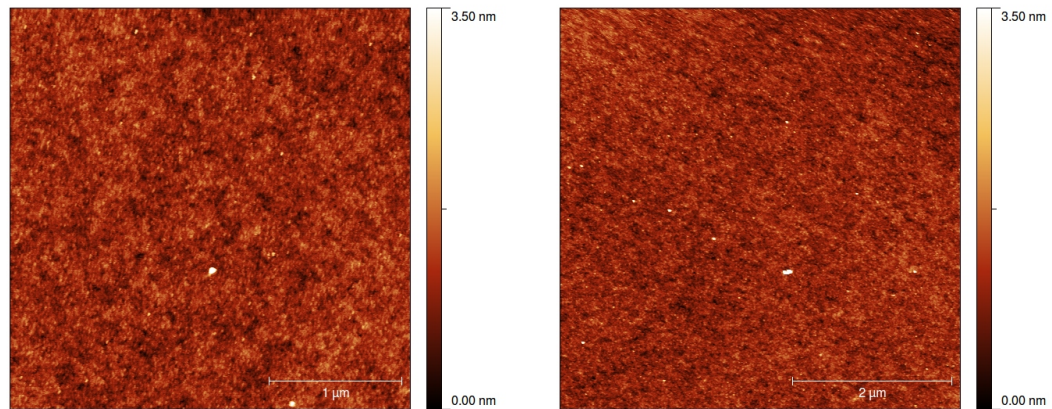
(c) 5 μm x 5 μm

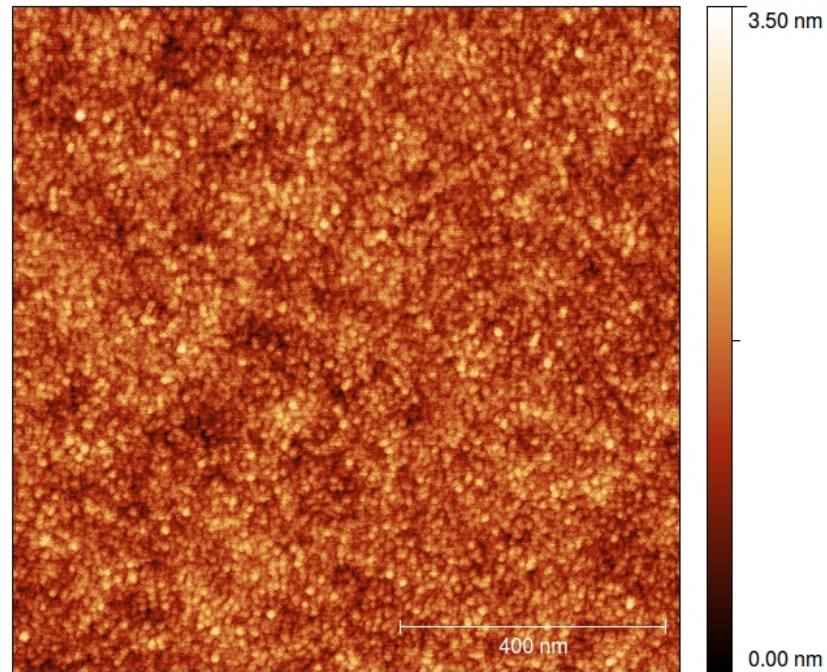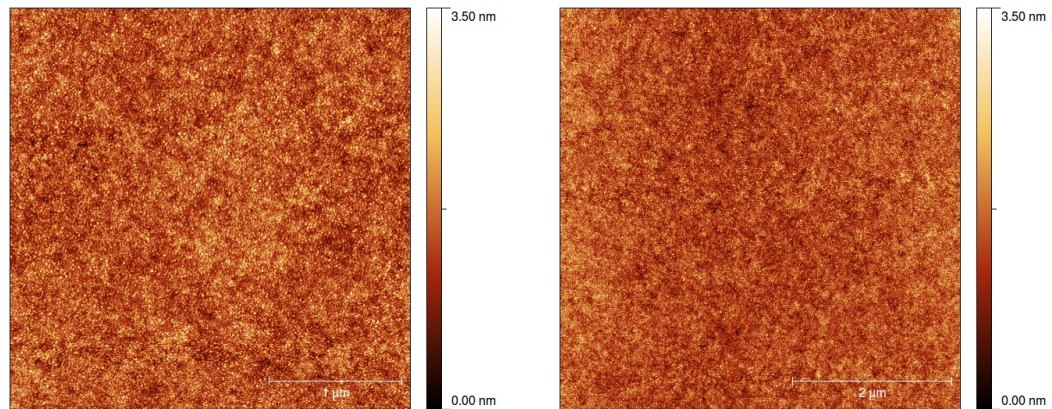Figure 5.19: 9 nm Si layer annealed at 700°C for 120 seconds.

Analysis of the nanoparticle distribution as a function of annealing duration, shown in Figure 5.20, reveals a similar pattern to the previously discussed nanoparticles. The shortest anneal of 30 seconds formed larger nanoparticles with a wide distribution. As the annealing duration increased to 60 seconds, these larger particle separated into smaller particles with a much more uniform radius and narrow distribution. For an annealing time of 90 seconds, the average nanoparticle radius continues to increase with narrow distribution about the mean. There is also a formation of larger particles that are well spread out that can be observe in the 3 x 3 and 5 x 5μm^2 scans of Figure 5.18. At an annealing time of 120 seconds, the nanoparticle radius continues to increase and the distribution begins to broaden.
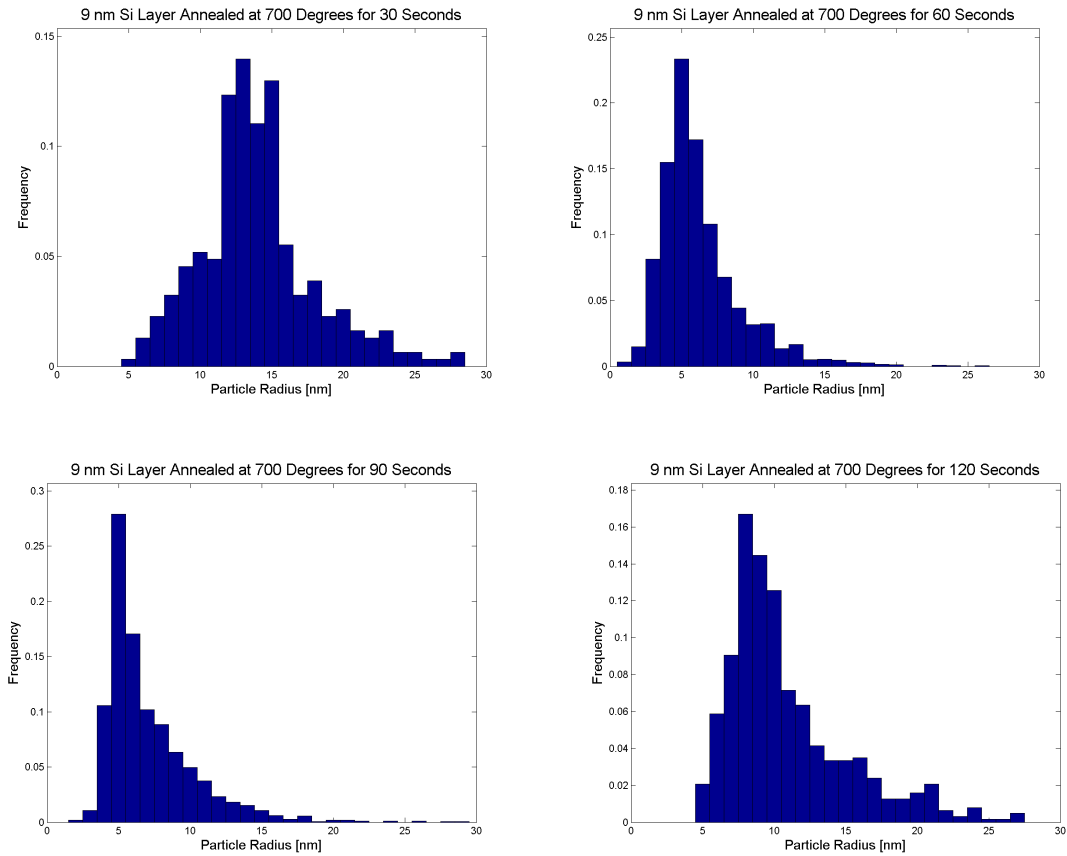
Figure 5.20: Particle Distribution as a Function of Annealing Duration. Nanoparticle radius distributions as a function of annealing duration using the threshold method. All anneals were done at a temperature of 700°C.

The average nanoparticle radius is summarized in Table 5.3 and shows that for the shortest annealing time of 30 seconds larger nanoparticles with a radius of approximately 14 nm were formed. As the annealing duration increased, these particles separated reducing the average radius to 6 nm. Continued annealing caused the smaller nanoparticles to merge together, increasing the average radius to almost 11 nm for a 120 second anneal.

Table 5.3: Average Nanoparticle Radius vs. Annealing Duration.

Annealing Duration [s]	Average Radius [nm]
30	14.78
60	6.28
90	7.13
120	10.93

5.4 Ellipsometry Results

The prepared nanoparticles were also analyzed using VASE to determine the nanoparticle composition in terms of their oxidation state as well as to draw connections between the ellipsometry data and the AFM data. We used an EMA approach similar to the one used by others.[25–27] As it is not clear to us how robust this approach is[28] we will link information obtained from the model fit to the deposition parameters and the results of the AFM measurements. The EMA was used to determine the ratio of amorphous to microcrystalline silicon in the sputtered film. Each sample was analyzed using VASE immediately after annealing. Samples were scanned using wavelengths of 0.209 - 1.0 µm and at angles of 55 - 75° in 5° increments.

Models were created for each sample group with the intent of minimizing both the mean square error (MSE) of the model to the measured Ψ and Δ data as well as to keep the complexity of the model low. The model consists of two layers: (1) a

Bruggeman effective medium approximation consisting of amorphous SiO_2 (SiO2-JAW), amorphous silicon (a-Si_Aspnes), and crystalline silicon (Si-JAW) that models the nanoparticle matrix; (2) a roughness layer consisting of 50% voids and 50% of layer 1 modeling the roughness of the samples after annealing (see Figure 5.21a). Although an attempt was made to fit all ellipsometric measurement data with this model, only the fits of the 3 nm samples resulted in a positive crystalline silicon fraction. We therefore conclude that the optical properties of the nanoparticles of our samples are best described by the optical properties of amorphous silicon of Aspen.

As the calculated volume fraction of crystalline silicon for the 6 and 9 nm silicon layer samples was negligible or negative, we simplified their model and removed the crystalline silicon out of it (Figure 5.21b). A diagram of the models used for the 3nm (Figure 5.21a) and the 6 and 9-nm samples (Figure 5.21b) are shown in Figure 5.21 below. Note that the model of Figure 5.21a contains 4 fitting parameters (ratio of crystalline silicon to amorphous silicon, ratio of amorphous SiO_2 to amorphous silicon, thickness of EMA, and thickness of roughness) and the model of Figure 5.21b contains 3 fitting parameters (ratio of amorphous SiO_2 to amorphous silicon, thickness of EMA, and thickness of roughness). This is not excessive compared to what other experts use in the field[29]
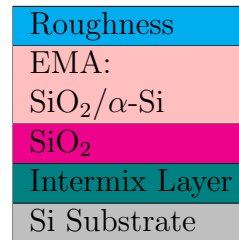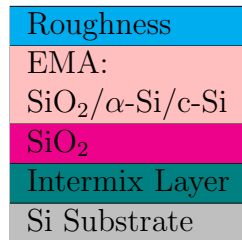
(a) 3 nm Silicon Layer Model   (b) 6 and 9 nm Silicon Layer Model

Figure 5.21: Optical Models. Model used for each silicon layer thickness.

The results of fitting the models to the ellipsometry data and their mean square errors are shown in Table 5.4 and Table 5.5. The main quantities of interest in these

tables are the volume fraction of silicon compared to silicon dioxide and the roughness as measured by the ellipsometer . In principle, both volume fraction and roughness can be determined independently from the two measured ellipsometric parameters (Ψ and Δ).[10] However, the problem of surface roughness characterization in transparent films with small refractive indices arises from measurement sensitivity, rather than the limitation of effective medium theories. In these transparent materials, it is generally difficult to distinguish the surface roughness layer from the bulk layer, because the refractive indices of these layers are similar.[30]

Analysis of the composition of the silicon layer after annealing reveals a general trend of a lower silicon dioxide volume fractions as the temperature increases. This decrease in oxidation is consistent with previous work, showing slower oxidation rates for smaller silicon nanoparticles caused by stress-induced suppression of the oxidization process. Referring back to Figures 5.13 and 5.20 as well as Tables 5.1 and 5.3, it can be seen that the 3 and 6 nm silicon layer samples produced larger particles with a wider distribution. It is also the 3 and 6 nm silicon layer samples that contain a higher volume fraction of silicon dioxide as compared to the 9 nm samples which had smaller particles with a more uniform distribution. The composition of the silicon nanoparticles, with the exception of the 6 nm samples, also match closely to previous work which determined that the composition of thermally roughened Si-SiO$_2$ contains 70-90% silicon.[10]

Further examination of the ellipsometric data, when compared to AFM data, shows that the roughness measured by VASE is similar to the average height of the samples as measured by AFM. This information is summarized in Tables 5.6 and 5.7. With the exception of the 3 nm samples, the roughness measured by spectroscopic ellipsometry tends to be about 0.2 - 0.3 nm larger than the average height of the samples.

Table 5.4: Ellipsometric Results. Ellipsometric results of nanoparticles as a function of silicon layer thickness and annealing temperature.

	Annealing Temp [C]	Roughness [nm]	EMA Thickness [nm]	EMA Composition			MSE
				α-Si (%)	c-Si (%)	SiO$_2$ (%)	
3 nm Layer	600	0.68	2.57	55.5	6.5	38.0	0.939
	700	0.43	2.15	66.4	6.1	27.5	0.994
	800	0.64	2.06	75.4	6.5	18.1	0.993
6 nm Layer	600	0.86	6.34	33.6		66.4	1.356
	700	1.05	5.92	37.9		62.1	1.217
	800	0.95	5.6	41.2		58.8	1.261
9 nm Layer	600	2.10	7.38	79.1		20.9	1.190
	700	1.71	7.56	79.0		21.0	1.093
	800	1.25	7.89	78.1		21.9	1.040

Table 5.5: Ellipsometric Results as a Function of Annealing Duration.

Annealing Duration [s]	Roughness [nm]	EMA Thickness [nm]	EMA Composition			
			α-Si (%)	c-Si (%)	SiO$_2$ (%)	MSE
30	1.38	7.38	76.4		23.6	1.119
60	1.71	7.56	79.0		21.0	1.093
90	1.92	6.78	81.5		18.5	1.003
120	1.34	7.35	76.7		23.3	1.117

9 nm Layer

Table 5.6: Comparing Ellipsometric Roughness and AFM Average Height.

	Annealing Temp [C]	VASE Roughness [nm]	AFM Average Height [nm]
3 nm Layer	600	0.68	1.170
	700	0.43	1.023
	800	0.64	1.032
6 nm Layer	600	0.86	1.253
	700	1.05	1.155
	800	0.95	0.969
9 nm Layer	600	2.10	1.464
	700	1.71	1.469
	800	1.25	1.367

Table 5.7: Comparison of Roughness as a Function of Time. Ellipsometric roughness compared to AFM average height.

	Annealing Duration [s]	VASE Roughness [nm]	AFM Average Height [nm]
9 nm Layer	30	1.38	1.265
	60	1.71	1.469
	90	1.92	1.685
	120	1.34	1.227

To better demonstrate the close matching of the ellipsometry data and the AFM data, a plot of the VASE roughness and AFM average height as a function of annealing duration is shown in Figure 5.22.
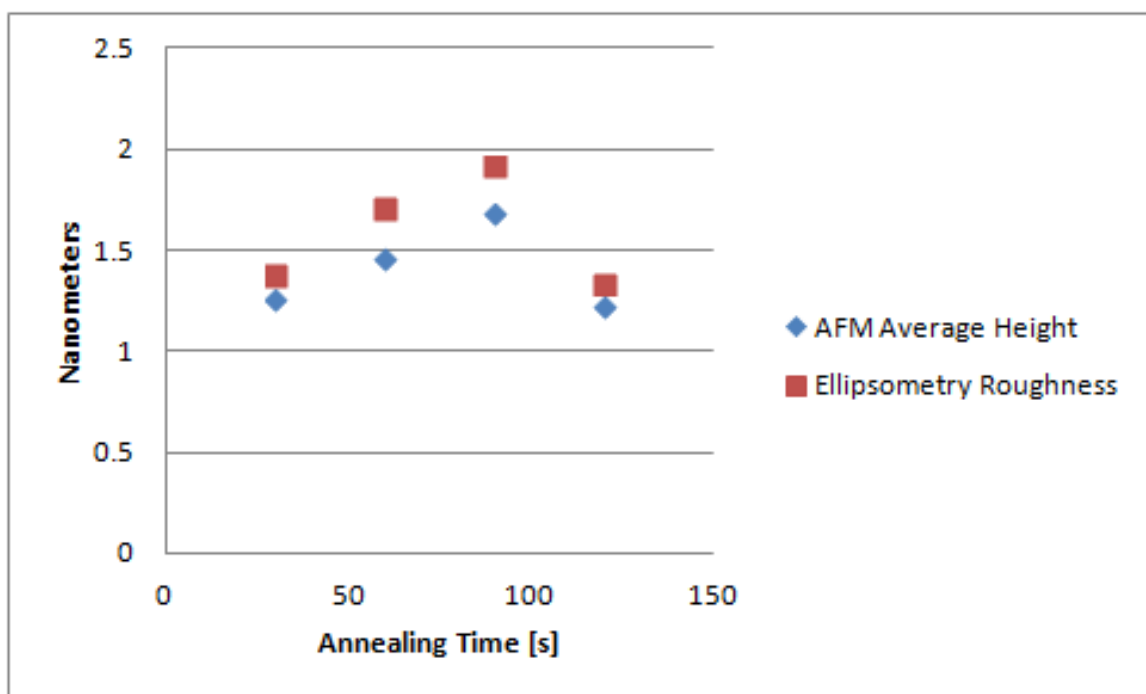
Figure 5.22: Plot of VASE Roughness and AFM Average Height. VASE roughness and AFM average height as a function of annealing duration.

CHAPTER 6

CONCLUSION

This work analyzed the formation of silicon nanoparticles produced by rapid thermal annealing of thin film silicon in an argon environment for various film thickness, annealing temperatures, and annealing duration. The results of these experiments showed that samples with a smaller initial silicon layer thicknesses and lower annealing temperatures produce larger average particle size and have a wide distribution. Samples with an initial silicon layer thickness of 3 nm that were annealed at 600°C produced particles with a range of radii from 2-20 nm and an average radius of 7.65 nm. The distribution of nanoparticle size becomes much more narrow for larger silicon layer thickness and the average size of the particles decrease. For samples with an initial silicon layer of 9 nm that were annealed at 600°C, the produced nanoparticles had a range of radii of 2-12 nm with an average radius of 5.97 nm. The average size of the nanoparticles increased as the annealing temperature and annealing duration increased.

The composition of these silicon nanoparticles were analyzed using variable angle spectroscopic ellipsometry, and it was found that the samples that exhibited a narrow distribution of small nanoparticles oxidized to a lesser extent than those with a wider distribution and larger nanoparticle size. Samples which had a 6 nm silicon layer thickness that were annealed at 600°C produced nanoparticles with an average radius of 8.19 nm with a wide distribution had a volume fraction of silicon dioxide of approximately 60% while samples with a 9 nm silicon layer thickness annealed at the same temperature produced a narrow distribution of nanoparticles

with an average radius of 5.95 nm had silicon dioxide volume fraction of only 20.9%. The surface roughness was also examined using VASE and was compared to measurements gathered by using atomic force microscopy. For most of the data, the two methods used to determine the surface roughness were very close with the ellipsometry measurements being approximately 0.2-0.3 nm larger than AFM average height measurements.

In order to build better optical models, future work on this project could include a coupled multi-sample analysis of the sputtered amorphous silicon before annealing. This could be used to better determine the optical properties of the silicon produced in the AJA magnetron sputtering system. This new optical spectra could be used to re-analyze the simulations on the annealed samples and build an even better model. Also, due to the difficulty of measuring the oxidation state and void fraction from solely spectroscopic ellipsometry data, future work should also include auger electron spectroscopy and x-ray photoelectron spectroscopy to better confirm the nanoparticle composition.

BIBLIOGRAPHY

[1] About silicon, `http://www.kemiwafers.com/about.php`.

[2] L. Pavesi and R. Turan, *Silicon nanocrystals: Fundamentals, Synthesis and Applications*, Wiley-VCH, Hoboken, NJ, USA, 2010.

[3] M. A. H. Khalafalla, H. Mizuta, and Z. A. K. Durrani, IEEE Transactions on Nanotechnology **2**, 271 (2003).

[4] K. Yano et al., IEEE Transactions on Electron Devices **41**, 1628 (1994).

[5] B. Legard, V. Agache, J. P. Nys, V. Senez, and D. Stievenard, Applied Physics Letters **76**, 3271 (2000).

[6] A. Bapat et al., Plasma Physics and Controlled Fusion **46** (2004).

[7] Y. Wakayama, T. Tagami, and S. Tanaka, Journal of Applied Physics **85**, 8492 (1999).

[8] G. Spencer, B. Anyamesem-Mensah, H. Galloway, A. Bandyopadhyay, and D. Frasier, Vacuum Science Technology A **29** (2011).

[9] B. Legrand, V. Agache, J. P. Nys, V. Senez, and D. Stievenard, Journal of Applied Physics **91**, 106 (2002).

[10] S. J. Fang, W. Chen, T. Yamanaka, and C. R. Helms, Journal of the Electrochemical Society **144**, 231 (1997).

[11] R. Okada and S. Lijima, Applied Physics Letters **58**, 1662 (1991).

[12] H. Hofmeister, F. Huisken, and B. Kohn, The European Physics Journal D **9**, 137 (1991).

[13] D. Yang, J.-N. Gillet, M. Meunier, and E. Sacher, Journal of Applied Physics **97** (2005).

[14] R. Behrisch, *Sputtering by Particle Bombardment: Physical Sputtering of Single-Element Solids*, Springer Berlin Heidelberg, Berlin, Germany, 1981.

[15] M. Ohring, *Material Science of Thin Films: Deposition and Structure*, Academic Press, San Diego, 2nd edition, 2002.

[16] S. Sultana, *RF Magnetron Sputtering system: Anelva Sputtering Unit Model SPF-332H*, Centre for Excellence in Nano-Electronics, Indian Institute of Science, Bangalore.

[17] Rapid thermal processing and rapid thermal anneal introduction, `http://www.ag-rtp.com/rapid-thermal-process-2.htm`.

[18] W. Yuan, Variable angle spectroscopic ellipsometry of inalp native oxide gate dielectric layers for gaas mosfet applications, Master's thesis, University of Notre Dame, 2009.

[19] J.A. Woollam Co., Inc., Lincoln, NE, *CompleteEASE Software Manual*.

[20] G. S. May and C. J. Spanos, *Fundamentals of Semiconductor Manufacturing and Process Control*, John Wiley and Sons, Inc., Hoboken, New Jersey, USA, 2006.

[21] Digital Instruments Veeco Metrology Group, Somerset, NJ, *Dimension 3100 Manual*.

[22] Atomic force microscopy, `http://www.nanoscience.com/education/afm.html`.

[23] The common afm modes, `http://www.chembio.uoguelph.ca/educmat/chm729/afm/details.htm#contact`.

[24] Afm artifacts, `http://www.afmhelp.com/index.php?option=com_content&view=article&id=65%3Aconvolution&Itemid=64`.

[25] S. Charvet, R. Madelon, F. Gourbilleau, and R. Rizk, Journal of Applied Physics **85**, 4032 (1999).

[26] T. D. Kang, H. Lee, S. Park, and S. L. J. Jang, Journal of Applied Physics **92**, 2467 (2000).

[27] P. Petrik et al., Journal of Applied Physics **87**, 1734 (2000).

[28] H. Fujiwara, J. Koh, P. Rovira, and R. Collins, Physical Review B **61**, 10832 (2000).

[29] C. Herzinger, B. Hohs, W. McGahan, J. Woollam, and W. Paulson, Journal of Applied Physics **83**, 3323 (1998).

[30] H. Fujiwara, *Spectroscopic Ellipsometry Principles and Applications*, John Wiley and Sons Inc, Hoboken, NJ, 2007.

VITA

Chad Lawrence Waxler was born on February 3rd, 1987 to Larry and Diana Waxler in Seguin, Texas. After graduating from Seguin High School in 2005, he entered Texas Lutheran University in Seguin, Texas. He graduated cum laude and received the degree of Bachelor of Arts in Physics in May of 2009. In August of 2009 he entered the Graduate College at Texas State University-San Marcos to pursue his Master of Science in Physics.

Upon graduating from Texas State, Chad hopes to pursue a career in the semiconductor industry.

Permanent Address: 779 Burges Street

Seguin, Tx 78155

This thesis was typed by Chad L. Waxler.